DEVELOPMENT OF A NOVEL METHOD TO PERFORM MORPHOLOGICAL MEASUREMENTS ON 3D MODELS OF THE CALCANEUS

MASTER THESIS | TECHNICAL MEDICINE

ALEXANDER WAKKER

DEVELOPMENT OF A NOVEL METHOD TO PERFORM MORPHOLOGICAL MEASUREMENTS ON 3D MODELS OF THE CALCANEUS

Alexander Wakker

Student number : 4384164

26-04-2022

Thesis in partial fulfilment of the requirements for the joint degree of Master of Science in

Technical Medicine

Leiden University ; Delft University of Technology ; Erasmus University Rotterdam

Master thesis project (TM30004 ; 35 ECTS)

Dept. of Trauma Surgery, Erasmus MC

October 2021 – June 2022

Supervisor(s):

Dr. M.G. (Mark) van Vledder, MD (EMC)

Dr. B.M.W. (Bart) Cornelissen, MSc (KT) (EMC)

Thesis committee members:

Prof. dr. M. (Maarten) van der Elst, MD, TU Delft (chair)

Dr. M.G. (Mark) van Vledder, MD, EMC

Dr. B.M.W. (Bart) Cornelissen, MSc (KT), EMC

Abstract

Currently, morphological measurements on conventional radiographs are used to assess calcaneal fractures. The two most commonly used angles for determining the degree of depression and displacement of such a fracture are Böhler's angle (BA) and the Critical angle of Gissane (CAG). However, conventional radiographs only provide limited amount of information and are increasingly being omitted, while CT-scans are increasingly being used as they contain much more information regarding fracture configuration and displacement. It is therefore important that morphological measurements can be performed using CT-scans. The purpose of this thesis were to design a novel method to perform semi-automated morphological measurements based on 3D models of the calcaneus. The results of the novel method were compared with conventional 2D measurements of the same calcaneus.

119 lateral foot radiographs and CT-scan of the same foot were obtained. The data consisted out of three populations: 40 non-fractured, 39 fractured and 40 reconstructed calcanei. Based on the CT-scans, 3D models were reconstructed through interactive segmentation processes. Measurements on the radiographs and 3D models were performed in a specially designed Graphical User Interface. Three observers measured BA and the CAG, after which they repeated the measurements after a minimum of one week. The inter- and intra-observers reliability were calculated separately for all three populations, using the intra-class correlation coefficient (ICC). Additionally, the frequency of consensus given an allowed discrepancy was calculated.

The ICC for inter- and intra-observer reliability of the 3D measurements showed an improvement for BA and the CAG for all populations compared with the ICC of the 2D measurements. The ICC for inter- and intra-observer reliability of the 3D measured BA ranged from 0.97 to 1.00, indicating an almost perfect agreement between the observers. For the CAG, the inter- and intra-observer ICC ranged from 0.89 to 0.92 and from 0.87 to 0.96, respectively. To achieve 80% consensus for the BA among the observers, an allowable discrepancy of 20°was needed for the 2D measurements, while only 5°was needed for the 3D measurements. To achieve 80% of consensus for the 2D CAG measurements, an allowable discrepancy of at least 20°was needed. For the fractured and reconstructed population, even an allowed discrepancy of 30°was needed. For the 3D CAG measurements, 80% of consensus was achieved with an allowable discrepancy of 5°, 20°and 10°for the non-fractured, fractured and reconstructed calcanei populations, respectively.

3D morphological measurements based on 3D models of the calcaneus showed better reliability and repeatability compared to the 2D measurements. However, the novel method of performing the measurements is not yet safe for use in clinical practice, as the measurements first should be validated. Nevertheless, the method is well suited to be employed as a reference for the development of further (semi-)automated methods to perform morphological measurements.

Contents

1 Introduction

1.1 Medical Background

Calcaneal fractures account for 2% of all fractures and is the most frequently fractured tarsal bone in the setting of trauma at 60%. Mainly calcaneal fractures are not open fractures which only occur in less then 10% of cases[1][2][3]. In 2010, the number of emergency admissions for foot and ankle injuries in the Netherlands was as high as 640 per 100.000 persons. In total this were around 25.000 ankle fractures, of which approximately, 2.000 were calcaneus fractures. These fractures are 2.4 times more common in men than in women. The average age at which male patients present themselves with a calcaneus fracture is between 20 and 39 years, while in females this is more evenly distributed across age cohorts[4][3][5].

The total cost for all patients with foot and ankle injuries was estimated at 161.9 million euros in 2010 for the Netherlands alone[5]. Besides, a Canadian study has evaluated indirect costs for both conservatively and surgically treated patients. The socio-economic cost for intra-articular calcaneal fractures were calculated. The calculations were based on the quality-adjusted life years(QALY), including time lost from work, complications and secondary arthrodeses. The average cost per surgically treated patient was 19.000 euros benefit of 2.50 QALYs. For the conservatively treated patients, the costs were 30.000 euros benefit from 2.43 QALYs[6].

Falls from height and motor crashes are the predominant mechanism of injury due to the axial force distributed throughout the calcaneus. Moreover, twisting/shearing events and jumping on hard surfaces can also cause a calcaneus fracture[3][7]. Calcaneal fractures can be divided into extra-articular and intra-articular types. Extra-articular fractures are in general less adverse and can mostly be treated conservatively. Intra-articular fractures account for 60-70% of calcaneal fractures, which in most cases require surgical treatment due to the displaced intra-articular fractures[5]. Fractures of the calcaneus are not life-threatening. However, these fractures are complex injuries that often require complex reconstructive surgery, especially after high energetic traumas[8]. Moreover, incorrect treatment of the calcaneus can lead to long-term and permanent disability.

After a trauma, the calcaneus is initially assessed based on conventional radiographs. Findings indicate the need for supplementary CT-scan to determine whether the calcaneus fracture should be treated conservative or operatively. The indication to perform surgery depends on the potential articulaire stepp-off and deformation of the hindfoot[9]. However, there are no reliable methods to perform morphological measurements based on CT-scans. This often makes it challenging for the surgeon to devise a preoperative planning. Intraoperatively, the reconstruction of the calcaneus is usually assessed based on fluoroscopy. However, fluoroscopy only provide limited amount of information regarding the progress of the surgery and whether the surgery is successful. Postoperatively and during follow-up, conventional radiographs are often omitted due to the limited amount of information. To assess the reconstruction of the calcaneus, a CT-scan is obtained for better visualization. However, since there is no reliable way to perform morphological measurements, it is not possible to obtain an objective description whether the surgery was successful.

Calcaneal malunion is a common complication that results in disability after conservative or incorrect treatment of a calcaneus fracture[10]. To treat a malunion, a correction osteotomy should be planned based on a 3D model of the calcaneus obtained from a CT-scan. If possible, the contralateral side is used as a template to assess how to perform the osteotomy. However, if a intra-articular calcaneal fracture occurs a patient represents himself in 10% of the cases with a bilateral calcaneal fracture[11]. If such a fracture occurs it is not possible to use the contralateral side as a template. For these cases, there is a need for an objective description of the morphology, or a statistical shape model to be able to determine the osteotomy. However, there are yet no reliable methods to do so. After the correction osteotomy, the result of the surgery should be assessed based on a CT-scan, which cannot be done reliably, as previously described.

1.1.1 Anatomy

Before it is possible to assess the extent of injuries to the calcaneus, it is essential to understand the normal anatomy (Figure 1). The calcaneus is the largest tarsal bone, located in the most posterior region of the foot and inferior to the talus, in a slight valgus position[8][12]. Numerous muscles and ligaments are attached to the calcaneus and contribute to its role in human bipedal biomechanics. Walking and running distribute external forces to the foot[7]. The calcaneus transfers most of the forces of the bodyweight to the ground and provides substantial leverage for the Achilles tendon, as can be seen in Figure 2[8][13]. The calcaneus can move relative to other tarsal bones by four articular surfaces. There are three superior surfaces, containing the anterior, middle, and posterior facets, that articulate with the talus, and one facet that articulates with the cuboid. The location of the middle facet is on the superior surface of the sustentaculum tali, which supports the head of the talus. The sustentaculum tali is the most stable part of the calcaneus and is connected to the talus by the talocalcaneal ligaments. The tendon of the flexor hallucis longus runs inferior of the sustentaculum tali, and produces a compressive force. These structures result that the sustentaculum tali is held in the correct position relative to the talus when a fracture occurs[14]. The joints between the calcaneus and the talus and between the calcaneus and the cuboid are called the subtalar, and calcaneocuboid joints, respectively[8]. The posterior facet, which is part of the subtalar joint, bears 75% of the axial force through the subtalar joint[15]. The subtalar joint provides essential foot motions such as eversion, inversion, dorsiflexion, and plantarflextion[16]. The calcaneocuboid joint is one of the least mobile intrinsic foot joints because the articular surface is relatively flat, with some irregular shapes. The calcaneocuboid joint can move in three distinct ways. These are inversion-eversion, medial-lateral rotation, and plantarflexion-dorsiflexion, with the most extensive movement to inversion and eversion[17][18]. The integrity of the shape and size of the calcaneus is of great importance for maintaining the normal function of the hindfoot. Changes in the anatomy due to fractures can affect the dynamic, kinetic, and static aspects of the foot[12].

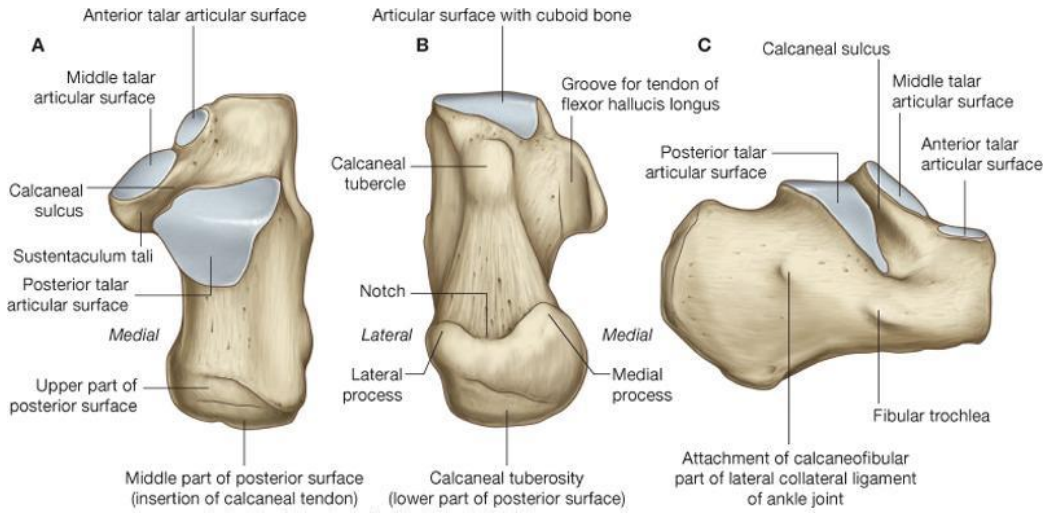

Figure 1: Anatomy of the calcaneus (a) Superior surface (b) Inferior surface (c) Lateral surface[19].

As described previously, most calcaneal fractures are caused by axial forces due to the bodyweight compressing on the talus. The talus transmits the force onto the medial side of the calcaneus, mostly resulting in a varus deformity. In addition, it often occurs that the high energetic force of the talus blows out the lateral wall of the calcaneus. Fractures caused by this force are mostly intra-articular. The fracture pattern depends on the magnitude and direction of the impacting force, foot position, muscular tone and mineral content of the bone[20]. The primary fracture line is created due to the direct axial force. If the energy of the impact

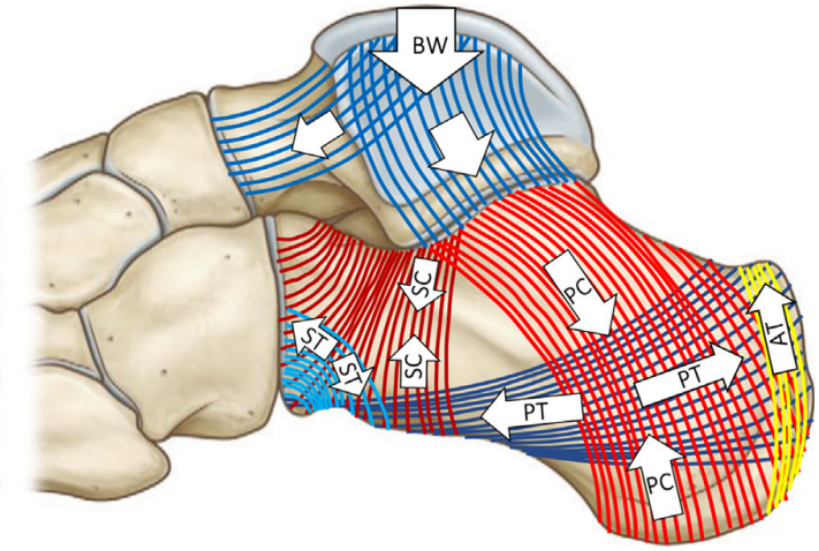

Figure 2: Force transfer of the calcaneus, Bodyweight on the talus (BW), primary compression lines (PC), secondary compression lines (SC), primary tensile lines (PT), secondary tensile lines (ST), Achilles tendon lines (AT)[13].

is not fully transferred, a secondary line is created. This fracture begins at the posterior aspect of the subtalar joint. Two types of fractures can occur: depression and the tongue-type fracture, as shown in Figure 3. In a depression-type fracture, the secondary fracture line runs downward posterior to the impacted posterior facet, only marginally involving the calcaneal tuberosity. A tongue fracture runs along the longitudinal axis through the tuberosity, resulting in a complex hindfoot deformity. The achilles tendon causes the superior part of the tuberosity to move cranially, which may cause the bone to puncture through the skin[14]. Because the sustentaculum tali mainly consists of cortical bone, it rarely occurs that a fracture line runs through this part of the calcaneus[21].

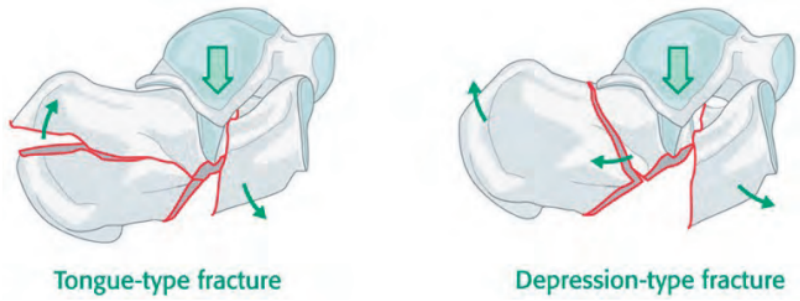

Figure 3: Essex-Lopresti classification[22].

1.1.2 Radiological assessment and morphological measurements

For the treatment of calcaneal fractures, the surgeon relies heavily on pre-operative imaging to diagnose and classify such a fracture. Visualization of these fractures is essential for devising an operative strategy. Currently, mainly radiographs and Computer Tomography (CT) scans are used for visualization, providing essential information about the fracture morphology. Translating 2D images into 3D situations in the surgeon's head poses a significant challenge in planning and executing the preconceived plan for post-traumatic bone deformities.

For diagnosis, treatment, and prognosis of calcaneal fractures, antero-posterior, lateral and axial radiological examinations of the foot are performed using X-rays. The most commonly used angles for determining the degree of depression and displacement of the subtalar joint are Böhler's angle (BA), and the Critical angle of Gissane (CAG)[23]. However, conventional radiographs only provide a limited amount of information regarding fracture configuration and displacement. For this reason, abnormalities on the conventional radiograph are an indication for making a CT-scan of the foot. This because CT-scan can be used to precisely analyze the fracture morphology (e.g., fracture size, number of fragments, degree of reduction and dislocation of the various fragments)[24]. All of these factors have to be considered for devising a treatment plan. Because most factors cannot be assessed on conventional radiographs, while this is possible on a CT scan, conventional radiographs are often omitted, especially during the post-operative phase and follow up.

Böhler's angle

BA is measured on a lateral viewed radiograph of the calcaneus. The angle is calculated by drawing a line from the most superior point of the posterior facet to the most superior point of the calcaneal tuberosity and a line from the anterior process to the posterior facet(Figure 4). This angle ranges between 20° and 40° in non-fractured calcanei bones[8][25]. Deviations from the angle indicate the degree of depression, displacement of the subtalar joint, and the extent of deformity between the anterior and posterior parts of the calcaneus. A fracture can lead the angle to become smaller, straighter and can even reverse the angle[8][26].

Critical angle of Gissane

The CAG is also measured on a lateral viewed radiography. The angle is specified by the intersection of two semi-lines on the calcaneal sulcus, one beginning at the processus anterior and the other along the posterior facet(Figure 5). In the literature, there is variation about the range of the normal CAG. Antony et al.[27], describes that the angle ranges from 130° to 145°, while keener et al.[8] states that the angle ranges from 120° to 145°. Deviations from the normal angle indicate the degree of depression, displacement of the subtalar joint and position of the ptc relative to the processus anterior[8]. Mostly, the angle becomes larger if the posterior facet is depressed due to a fracture[8][28].

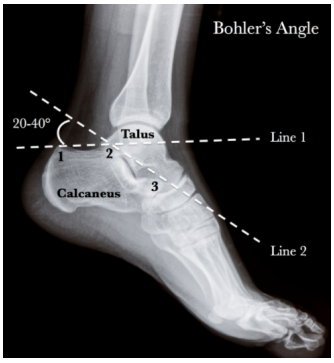

Figure 4: Böhler's angle[25].

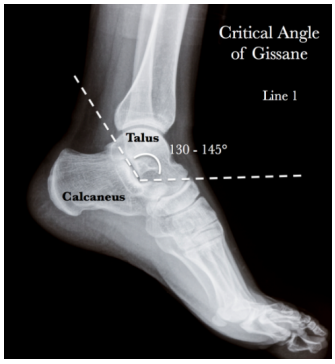

Figure 5: Critical angle of Gissane[27].

Axial view

When there is a clinical suspicion of a fracture, due to an abnormal BA, CAG or potential fracture line, an axial view of the foot is obtained to evaluate the lateral and medial walls of the calcaneus and to visualize the posterior and middle facet of the subtalar joint(Figure 6). In addition, the varus/valgus deformities can be determined based on visual inspection. An axial viewed image of the foot is made by letting the patient extend their leg whilst sitting on a table. The foot is held in 90° dorsiflexion, and the x-ray beam is directed on the plantar aspect of the foot at an angle of 40°[23].

Figure 6: Axial view of the foot[23].

Computer Tomography

Due to the high energy axial force, calcaneal fractures are often comminuted fractures, which sometimes consist of up to 5 main fragments[20]. These fractures often cannot be assessed with conventional X-rays because the fracture lines are often not visible. For this reason, a CT-scan of the calcaneus is made to analyze the fracture morphology precisely. However, even with a CT-scan, it is sometimes extremely difficult to understand the morphology and visualize all fractured and reconstructed calcanei. This is because high energetic traumas causes large parts of the calcaneus to be displaced by the impact of the talus on the calcaneus. Consequently, the contour of the calcaneus sometimes cannot be properly visualized. One reason for this is that a CT-scan consist of multiple 2D images existing in a 3D environment, making it difficult to translate the 2D images into 3D situations. In addition, it is difficult to perform morphological measurements on CT-images because when measuring on CT-images, often only a single slice (2D) of the 3D image is used. If the measurement is performed on another slice of the CT-scan, the measurement would probably not match. Because measurements on both conventional radiographs and CT-scans can be challenging, some studies developed a new method to perform morphological measurements on 3D models of the calcaneus based on CT-scans[29][30][31][32][33][34]. These 3D-models give a much greater understanding of the complex fracture morphology, allows accurate planning for open reduction and internal fixation(ORIF) of the calcaneus, can be used for education purposes and to perform morphological measurements.

1.2 Technical Background

1.2.1 Segmentation

Segmentation is a technique used to divide data sets into multiple image segments to change the representation of image in a more understandable way. In this process, pixels 2D and voxels 3D are assigned labels that share the same properties. Segmentation is used to identify different bone structures, and to distinguish soft tissue from bone structures. Hounsfield Units(HU), which is proportional to the degree of attenuation/absorption coefficient of radiation within tissue, is commonly used to divide different structures. This is done because HU is universally used in CT-scanning to express CT-numbers in a standardized and convenient form[35].

Thresholding

Thresholding is a technique of segmentation whereby pixels or voxels with a certain HU are divided into signal and background. Tissue within the given range is labeled as signal (this is the mask), while tissue out of the given range is labeled as background. Choosing the proper threshold is therefore important. A wrongly picked threshold could significantly slow down the segmentation process. Factors such as image quality and type of tissue could influence the preferred threshold. Bone has a HU that ranges between 200 and 3000 HU. For cancellous bone this is between 200 and 400, while for cortical bones this is between 500 and 3000 HU[36][37][36]. An example of a segmentation of the lower extremities with the predefined bone threshold in Materialise Mimics, version 24.0 (Materialise, Leuven, Belgium) can be seen in figure 7.

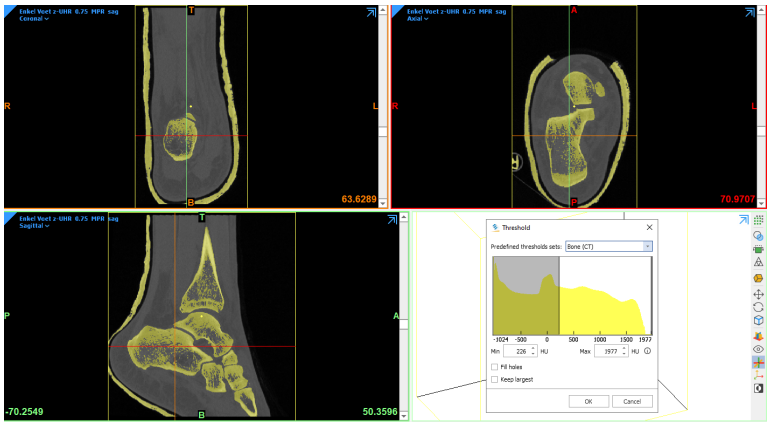

Figure 7: Highlighted yellow mask after using the predefined threshold for bone structures.

Separation of structures

The purpose of segmentation is often to separate different structures. The easiest and fastest technique is region growing, which is a voxel-based segmentation method. This tool can be used to separate spatially connected regions. To do so, a seed point has to be selected on the bone area covered with the target mask. This action will add all connected regions to this mask, while excluding any unconnected regions. To distinguish the calcaneus from, for example, the talus, the seed point needs to be selected on the calcaneus. However, it can occur that there are connections between these structures, which would result that the structures are not separated. If so, a function called split mask can be used to split the target mask into two or more masks. First, the structure(s) intended to segment should be marked in multiple slices, after which, the other structure(s) should be marked in multiple slices. The worse the distinction between the structures, the more slices should be marked. When marking the areas, it is important that the markings are close to the edge of the structures that need to be seoarated. Figure 8, shows an example of the calcaneus being distinguished from the other structures using the split mask function.

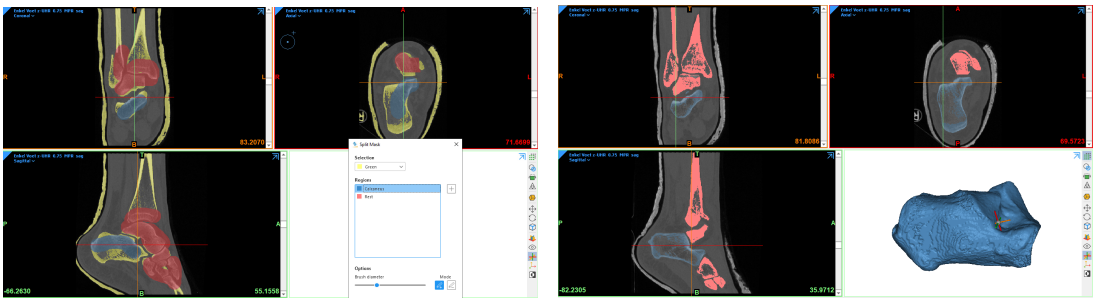

(a) Indicating the different structures.

(b) Result of the split mask tool.

Figure 8: Separation of the calcaneus by mean of the split mask tool.

Modify and finalize model

After initial thresholding and separation of structures, the anatomy of interest is usually not completely covered by the mask. To include these voxels, multiple different modify tools can be used to do so. The most convenient tool for filling these holes and cavities is the smart fill tool, which is used for global and local filling. First, the global filling should be used. With this step, a hole closing distance should be picked, allowing the user to define the size of the holes that should be filled. By using global filling, an algorithm will look at the entire mask and will try to fill all the holes and cavities, with the size of the picked hole closing distance. If still not all holes and cavities are filled, then local filling should to be used, which allowed the user to manually fill the holes and cavities. This process will result in a solid mask that corresponds to the target mask. Figure 9 shows an example of this process, where the filled holes and cavities of the calcaneus are indicated by the green coloration.

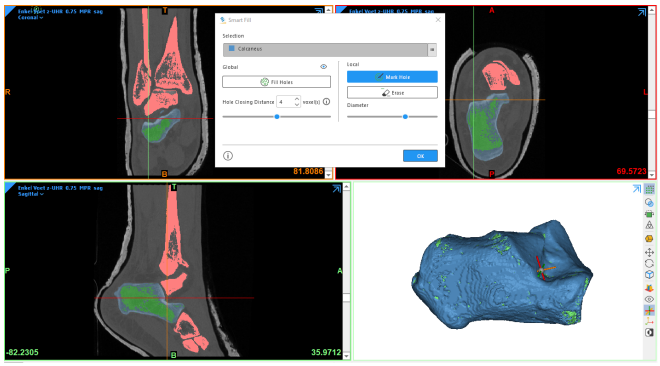

Figure 9: Blue indicates the calcaneus before modifying the mask, and green shows filled holes and cavities by the smart fill tool.

1.2.2 Statistical Shape Model

A statistical shape model (SSM) is a model that describes a collection of similar objects in a compact way. Gaussian Process Morphable Models (GPMMs) are the framework for generating the SSM. These GPMMs are a generalized form of point distribution models (PDMs), which is a model for representing the mean geometry of a shape as well as their variation in shape[34]. In addition, these models can be used for anatomical orientation purposes, such as creating standard anatomical planes for a dataset of models. Lüthi et al.[38][39] described the mathematical background and processing of GPMMs.

Principal Component Analysis

Principal component analysis (PCA) is an essential tool for generating a shape model. To create such a model, large data sets, with often more than 100 models, have to be compared. This is often difficult to interpret because the dimensionality of the dataset are extremely high. PCA is a technique that is used for reducing the dimensionality of a dataset. This increases the interpretability, but at the same time minimizes the loss of information such as the statistical variation in a dataset[40]. PCA is used to create simplified 3D models containing only the most important anatomical features

Registration

Image registration is a process of aligning two or more images, which is needed for PCA. The goal with this process is to find the optimal transformation to spatially align the structures of interest. A predefined moving image will be aligned with a predefined fixed image. Deformation of the moving image can be performed using different transformations such as translation, rigid transformation, affine transformation and non-rigid or deformable transformations.

1. Translation is a transformation only using a translation vector.
2. Rigid transformation allows the moving image to be translated and rotated using a translation vector and moving matrix.
3. Affine transformation uses the same vector and matrix as rigid transformation, but also allows scaling and shearing of the moving image.
4. Non-rigid or deformable transformations is the most complex transformation. It can change the size or shape, or both size and shape, of the moving image.

Iterative Closest Point

An Iterative Closest Point (ICP) algorithm is used to align two points of clouds (2 models). These models can consist out of 2D or 3D points. These algorithms can be based on different type of transformations, as discussed previously. The purpose of this algorithm is to minimize the sum of squared difference between the corresponding point models, by aligning a moving model to a fixed model. To minimize this, first the nearest neighbor approach is used so that all the points of the moving model are linked to the closest point on the fixed model, this is called the data association step. The second step of the process is to compute the transformation based on the data association step. The transformation is first performed by aligning the models by computing the center of mass of the models. The second step of the transformation is by rotating the moving model, so it would match the fixed model. After these steps, the data association step and transformation step are repeated until the square error between the corresponding points is below a minimum, the datasets are converged or if a certain number of iterations are performed[41].

1.2.3 Graphical user interface

A Graphical user interface (GUI) is a type of interface though which users can interact with, for example, visual components on an electrical device. A program called MeVisLab can be used to design these interfaces. MeVisLab works with graphical representations of models that have different function for image interaction, image visualization and image processing. The three basis module types are: MeVis image processing Library (ML) modules (blue), Open inventor Modules (green) and Macro Modules (orange), which are distinguished by their colors (Figure 10).

The ML modules are used to load, save images and view image properties, but can also be used to process voxels of the loaded images. With the Open inventor Modules, visual scene graphs can be created and modified. The Macro modules are used to combine other module

Figure 10: Examples of different modules.

types, allowing for implementing hierarchies and scripting interactions (Python). Already existing macro's have internal networks, which give a better visualization of the working process of the module.

Modules have different type of connectors, which show how different modules can be connected to each other. These are the data connections, which have the output on top of the model and the input at the bottom. There are also parameter connections, which are connections between different modules that are not connected with the connectors, but with lines (Figure 11).

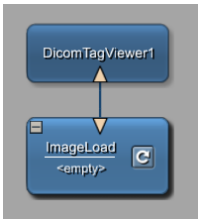

(a) Data connection

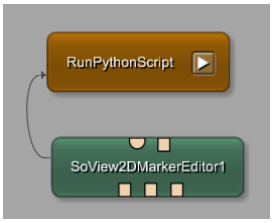

(b) Parameter Connection

Figure 11: Possible connection between modules

1.3 Literature study

The literature review preceding this thesis described current practices and challenges in assessing calcaneus deformities. This review investigated the the reliability of performing 2D radiographic measurements of BA, CAG and varus/valgus angulation. In addition, it was also investigated whether there are new methods to perform these measurements based on CT-scans or 3D models of the calcaneus.

Initially, after trauma, the calcaneus is assessed using lateral and axial radiographs for diagnosis and management of a calcaneus fracture. On the lateral radiographs, BA and the CAG indicate the degree of depression and displacement of the subtalar joint. The axial radiograph is used for visual inspection of the lateral and medial wall and for potential varus/valgus angulation of the calcaneus. However, for BA and the CAG, the inter- and intra-observer reliability has been reported limited in several occasions[26][42][43][44][45][46][47][48]. In addition, there is no robust method for determining varus/valgus angulation.

Findings on lateral and axial radiographs indicate the need for a preoperative CT-scan. This because a CT-scan contains additional information regarding the fracture morphology (e.g., fracture size, number of fragments, intra-articular step-off, fracture location, dislocation of the various fragments, degree of depression of the ptc and position of the ptc relative to the processus anterior)[24]. Intraoperatively, fluoroscopy is usually used to assess the progression of the surgery using the previously mentioned morphological measurements, while the measurements are not reliable. Intra- and postoperative CT-scans is increasingly being used because these scans contain much more information. However, there are no reliable methods

to perform morphological measurements based on CT-scans.

By using all data available from CT-scans, it is possible to create 3D models of the calcaneus, which offers the possibilities to perform morphological measurements on these 3D models. For this reason, several studies have developed novel methods to perform morphological measurements on 3D models of the calcaneus in which the BA and CAG are described. Despite the promising results in their studies, there is currently no standardized method to describe the morphology of a fractured or deformed bone based on 3D models[29][30][31][32][33][34]. The currently designed methods for morphological measurements were only tested based on non-fractured calcanei, except Qiang et al.[31] who performed measurements on reconstructed calcanei. The designed methods are yet no optimal and there are still areas of improvement, such as; (semi-)automated landmark placement, an easy-to-use software tool to perform morphological measurements and determining the orientation based on Statistical shape models or based on registration.

In conclusion, measuring BA and the CAG is not reliable and there is no robust method to measure the varus/valgus angulation based on 2D radiograph images of the calcaneus. As a result, these techniques are increasingly being omitted and CT-scans are increasingly being used. However, it is not possible to perform reliable morphological measurements based on CT-scans. For this reason, studies have developed novel methods to performing morphological measurements based on 3D models, which show promising results. However, there are still areas of improvement before these methods can be used in clinical practice.

2 Objectives

The primary objective of this thesis was to develop a novel method to perform semi-automated morphological measurements based on 3D models of the calcaneus to improve the inter- and intra-observer reliability. The two main morphological measurements examined were Böhler's angle and the Critical angle of Gissane. These measurements were also performed on conventional 2D radiographs of the same foot, as the results had to be compared with the novel designed method, to determine whether the novel method improved the inter- and intra-observer reliability.

The secondary objectives were;

1. to construct a Statistical shape model of the calcaneus, for anatomical orientation purposes, and;
2. to construct a semi-automated landmark placement tool in the Graphical User Interface, and;
3. to determine the frequency of consensus given an allowed discrepancy for intra- and inter-observer measurements on conventional radiographs and 3D-models of the calcaneus, and;
4. to determine the mean morphological 2D and 3D measurements of the Böhler's angle and Critical angle of Gissane

3 Methods & Materials

This study a single-center pilot study, using existing conventional radiograph and CT-scans of patients with non-fractured, fractured and reconstructed calcanei seen at the Erasmus MC between 2006 and 2021. The study was waived from IRB review because there was no more than minimal risk for using the data of the patients. To be eligible to participate in this thesis, the data had to meet the following criteria:

Inclusion criteria

1. Conventional radiograph and CT-scan of a non-fractured calcaneus of the same foot, or;
2. Conventional radiograph and CT-scan of a fractured calcaneus of the same foot, or;
3. Conventional radiograph and CT-scan of a reconstructed calcaneus of the same foot.

Exclusion criteria:

1. Data used from a patient younger than 16 years.
2. Image quality too poor, making it impossible to segment the data of the-CT scans.
3. Time between the taken conventional radiograph and CT-scan $>$ 6 months.
4. Extra-articular fractures for the fractured population.
5. Subtalar arthrodesis for the reconstructed population.

Before using the data, all data were anonymized by an anonymization service at the Erasmus MC. The data were then available for download via XNAT (1.8.3), a secure environment for downloading the anonymized data.

The sample size needed to determine the intra- and inter-observer reliability was calculated using an online Intra-class Correlation Coefficient (ICC) hypothesis testing calculator[49], which used a method developed by Walter et al.[50]. The minimal sample size for each population was calculated at 37 calcanei. The sample size was calculated assuming the following variables: 3 observers, significance level of 0.050, power of 0.900, minimum acceptable reliability of 0.65, expected reliability of 0.85 and potentional drop-out of 10%. Bonett et al.[51], also calculated the sample size required for the intra-class correlation with desired precision. They calculated that at least 36 samples were required to obtain an exact confidence interval when three observers perform the measurements.

3.1 Data

A total of 119 lateral foot radiographs and 119 foot CT-scans of the same foot were collected for the comparison between the 2D and 3D measurements. The lateral radiographs and CT-scans for the measurements consisted out of 40 non-fractured, 39 fractured and 40 reconstructed calcanei. For creating the Statistical shape model(SSM), an extra 48 non-fractured calcanei CT-scan were included[52]. The investigator {AW} who did not participate in the measurements obtained all the data, and prepared all the materials before the observer could perform the measurements of BA and the CAG. The measurements were performed in a therefore designed GUI (Appendix A) by a consultant in trauma surgery, fellow in trauma surgery and registrar in trauma surgery. All observers had prior experience in performing 2D morphological measurements on the calcaneus.

3.2 Data Processing steps

Before the observers could perform the 2D and 3D measurement in the GUI, a number of processing steps with the CT-scans were required. In addition, a few algorithms had to be created. First, 3D models were created based on the CT-scans. Thereafter, the orientation of the 3D models were determined by mean of anatomical planes, which were constructed with two different methods. The first method used landmarks on the sustentaculum tali to reconstruct the anatomical planes. The second method was based on the anatomical planes of the SSM of the calcaneus. All calcanei models were registered with the SSM, resulting that all models had the same orientated anatomical planes. Furthermore, a semi-automatic landmark placement algorithm was created, which had to be implemented in a GUI. Finally, a script had to be implemented in the GUI that calculated the measurements by mean of the coordinates of the placed landmarks.

3.2.1 3D models

A total of 88 non-fractured, 39 fractured and 40 reconstructed calcanei were segmented with Materialise Mimics, version 24.0 (Materialise, Leuven, Belgium). For the segmentation, the threshold was set between 226 HU and the maximum HU for the given CT-data. After segmentation, the next step was to create 3D objects of the masks. To be able to use the 3D object in different programs, the object were saved as STL files, which are files that store information regarding the 3D objects. Before the objects were saved, they were first wrapped, after which the object were smoothed. This was done to ensure that STL-files were not too large and so that there were no loose and protruding voxels around the 3D objects. These objects were then exported to Materialise 3-matic, version 16.0 (Materialise, Leuven, Belgium) to remove spikes with the remove spike tool. Lastly, the models were saved as STL-files. The workflow of creating 3D models can be seen in figure 12.

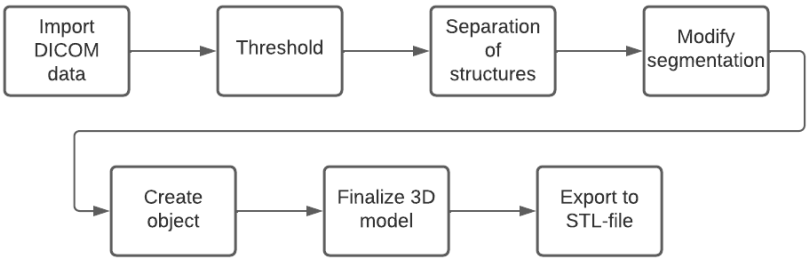

Figure 12: Workflow of the segmentation process

3.2.2 Statistical shape model

All non-fractured 3D left and right calcanei models were used to create the statistical shape model (SSM). Thereafter, the SSM was used for anatomical orientation purposes. All the left calcanei were mirrored to represent the right calcaneus. To create the SSM, all calcanei were aligned and expressed in the same topology. This means that all the meshes of the calcanei models were positioned on top of each other in the same world coordinate system, with the same number of vertices, faces and edges (Figure 13).

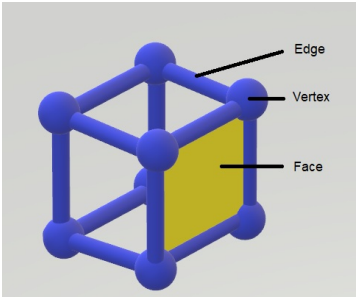

Figure 13: Example of a Mesh object.

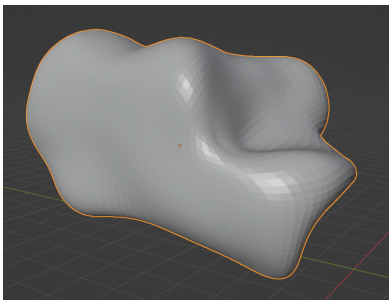

Figure 14: Template of the calcaneus.

The first step was to create a template of the calcaneus where the vertices, faces and edges were equally distributed across the template. This template was modeled using Blender® (3.0.1), using the sculpting workspace, resulting in a schematic representation of the calcaneus (Figure 14). The workflow of generating an SSM can be seen in Figure 15.

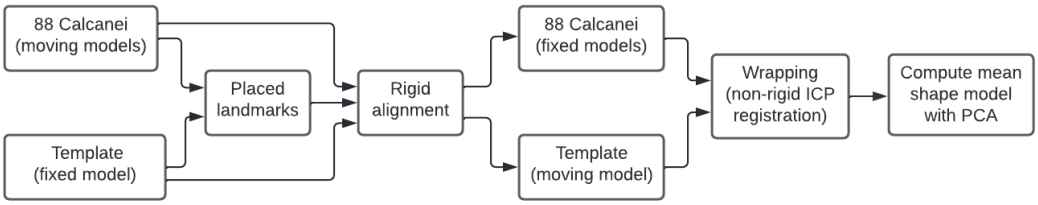

Figure 15: Statistical Shape Model workflow.

The second step was to perform a rigid transformation to align all calcaneal models (moving models) on top of the template model (fixed model). To properly perform this transformation, a total of 3 anatomical landmarks were placed on the template model that corresponded with the same anatomical landmarks on the calcaneal models. The anatomical landmarks were: the sinus tarsi, most superior point of the calcaneal tuberosity and the most medial part of the sustentaculum tali (Figure 16).

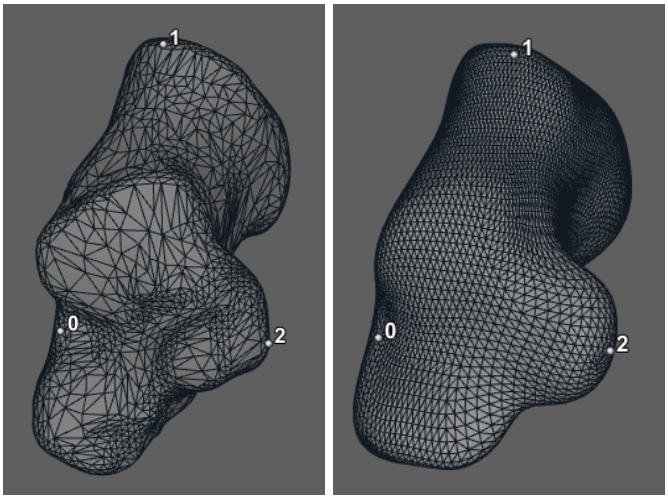

Figure 16: Placed anatomical landmarks for the rigid transformation. Left: moving calcaneal model, right: fixed SSM calcaneal model.

Thereafter, a non-rigid ICP registration was performed. With this transformation, the template model (moving model) was wrapped around each of the 88 calcanei models (fixed model) (Figure 17). This resulted that all 88 calcanei models were expressed in the same topology at the same location in the world coordinate system, identifying each point of the template models with the corresponding point on each of the calcaneal models. This allows pointwise calculation of the mean and variance for the SSM through PCA[34]. Both transformation steps were performed using R3DS Wrap(2021.11.3).

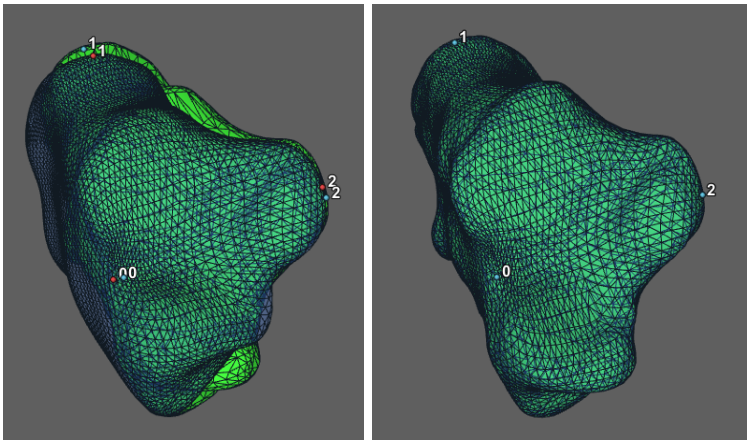

Figure 17: Before and after non-rigid ICP registration, left and right, respectively.

The last step was to compute the mean shape model of the calcaneus. This was performed using an open access library of Python(3.9) called Menpo3D(v0.8.0). With this library, first a PCA model was generated from all the calcaneal models with the same topology. Thereafter, the mean shape of the calcaneus was determined by iteratively calculating the minimal distance between the models in the PCA model. Lastly, mean right generated SSM was mirrored to reflect the left SSM.

3.2.3 Orientation

The orientation of the lateral radiographs only had to be adjusted for 2 images, as they were placed upside down. Based on a rotation function in MeVisLab, the 2D images were rotated 180°.

After creating the 3D calcanei models for 3D measurements, the models could not be used directly for morphological measurements. This was because the CT-scans were taken with different scanners and the foot position was inconsistent during the CT-scans. As a result, the 3D models were scattered throughout the world's coordinate system. To construct a consistent measurement standard, it is necessary to first determine the orientation of the models. For this reason, two methods were constructed to determine the orientation based on anatomical planes.

Method 1

The first method was designed based on landmark placement on the sustentaculum tali. This structure is the most stable part of the calcaneus, which is held in the correct position by the tendon of the flexor hallucis longus and the talocalcaneal ligaments[14]. Because a fracture line rarely runs through this portion of the calcaneus and remains in place after a calcaneal fracture, it was hypothesized that the sustentaculum tali could be used to reconstruct the anatomical planes. For the reconstruction of the anatomical planes, three landmarks were placed on the surface of the sustentaculum tali. The first two landmarks were positioned horizontal next to each other based on the anterior-posterior(AP) view. The third landmark was placed between and below the other landmarks. These landmarks were used to create two 3D vectors, which

is an object that has both a direction and a magnitude. By mean of the two vectors, first, the 3D cross product was calculated with equation 1, which is the normal vector of a plane. Thereafter, the 3D dot product was calculated with equation 2. The results of equation 1 and 2 were used to construct the plane equation on the sustentaculum tali, which was written in the form as shown in equation 3.

$$\vec{a} \times \vec{b} = |\vec{a}||\vec{b}| \sin\theta \hat{n} \tag{1}$$

Two Dimensional Dot Product

$$\vec{p} \cdot \vec{q} = \langle p1, p2 \rangle \cdot \langle q1, q2 \rangle = p1 \cdot q1 + p2 \cdot q2$$

Three Dimensional Dot Product

$$\vec{p} \cdot \vec{q} = \langle p1, p2, p3 \rangle \cdot \langle q1, q2, q3 \rangle = p1 \cdot q1 + p2 \cdot q2 + p3 \cdot q3$$

$$\vec{p} \cdot \vec{q} = |\vec{p}|\,|\vec{q}| \cos\theta \tag{2}$$

$$Ax + By + Cz = D \tag{3}$$

The placed landmarks and constructed plane on the sustentaculum tali can be seen in (Figure 18). To construct the axial and sagittal plane based on the sustentaculum plane, the sustentaculum tali plane had to be rotated using the combination of rotation matrices (equation: 4, 5 and 6). The axial and sagittal axis were defined by rotating the sustentaculum plane with 90° around the coronal axis and 45° around the axial axis, respectively (Figure 19).

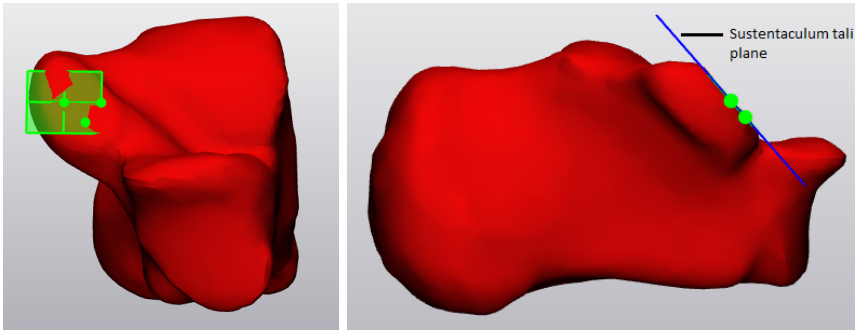

Figure 18: Example of selected landmarks on the sustentaculum tali, used to construct the sustentaculum tali plane.

$$Z - axis = \begin{bmatrix} \cos\theta & -\sin\theta & 0 \\ \sin\theta & \cos\theta & 0 \\ 0 & 0 & 1 \end{bmatrix} \tag{4}$$

$$X - axis = \begin{bmatrix} 1 & 0 & 0 \\ 0 & \cos\theta & -\sin\theta \\ 0 & \sin\theta & \cos\theta \end{bmatrix} \tag{5}$$

$$Y - axis = \begin{bmatrix} \cos\theta & 0 & \sin\theta \\ 0 & 1 & 0 \\ -\sin\theta & 0 & \cos\theta \end{bmatrix} \tag{6}$$

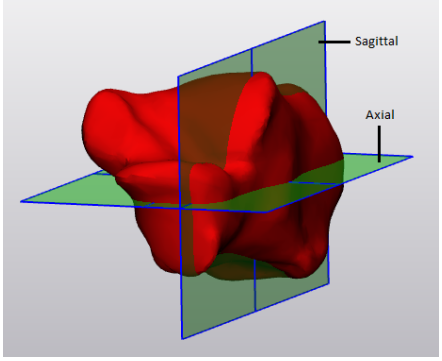

Figure 19: Sagittal and Axial plane based on a calcaneus.

This method for constructing the axial and sagittal plane had to be validated before the observer could use this method in the GUI. The observers had to indicate the points on the sustentaculum tali them-selves before selecting the points for the morphological measurements. If the observers did not correctly indicate these three points, the orientation of the planes would not be reliable. This could lead, for example, to a sagittal plane being placed obliquely through the calcaneus, which in turn can influence the performed measurements. For this reason, a total of 30 calcanei were used to validate this method. For all these calcanei, images of the constructed axial and sagittal plane were created, which were subsequently assessed by a radiologist. The radiologist determined if the planes were defined correctly.

Method 2

For the second method, anatomical planes were constructed based on the right and left SSM model of the calcaneus using 88 non-fractured calcanei. The sagittal and axial planes were determined on both calcanei in collaboration with an experienced radiologist. The anatomical planes of the right and left SSM model of the calcaneus were considered as the standard orientation. As described previously, the other 3D calcanei models were registered to the same position in the world coordinate system as the SSM models. The alignment of the models were not performed by the observers, but were performed prior to the morphological measurements. The following steps were performed to align the models. To obtain a correct alignment, two registration methods were combined. The first step was an N-point registration based on three anatomical landmarks on the sustentaculum tali. Like method 1, this structure was used because in almost all cases it remains intact and in position after a calcaneal fracture, which makes this structure ideal for selection of anatomical landmarks. The landmarks were placed at the same anatomical locations on both the SSM model and on each of the calcaneal models (Figure 20a). The locations were: the most superior part of the sustentaculum tali, the most medial part of the sustentaculum tali and the transition between the sustentaculum tali and the processus anterior. After selecting the anatomical landmarks, a rigid registration was performed based on the these landmarks, re-positioning the calcaneus at the location of the SSM model. However, with an N-point rigid registration, most models did not overlay properly, as can be seen in Figure 20b. For this reason, after the N-point registration, a global rigid registration was performed, which resulted in the final alignment of the models (Figure 20c). Figure 21 shows how all the non-fractured, fractured and reconstructed calcanei were aligned on top of each other in the same world coordinate system, including the 'standard' anatomical planes. The orientation of the calcanei were validated based on visual inspection.

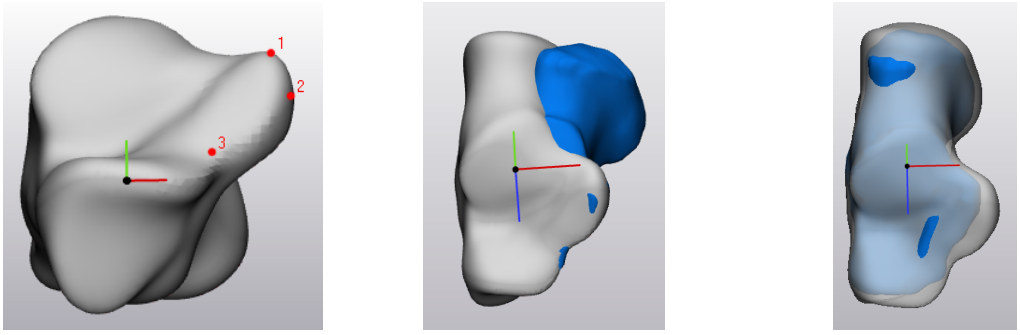

(a) Landmarks for registration (b) N point registration (c) global registration

Figure 20: Detailed procedure for registration of a right calcaneal model (blue) with the right SSM model of the calcaneal (gray).

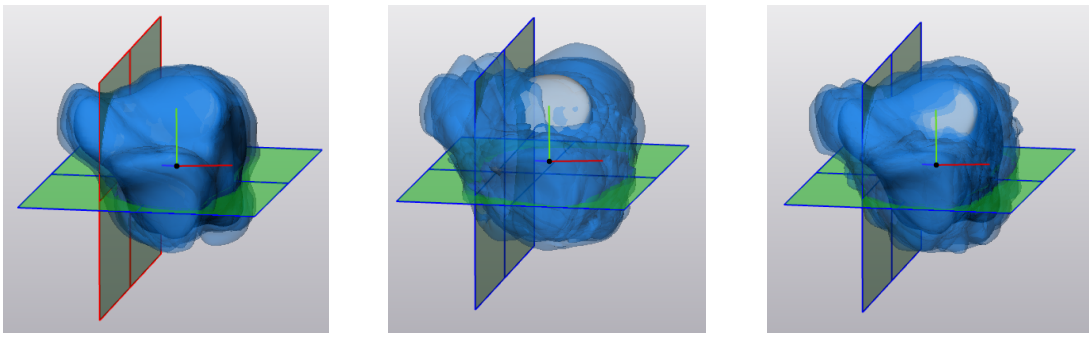

(a) Non-fractured calcanei (b) Fractured calcanei (c) Reconstructed calcanei

Figure 21: Final alignment of all left calcanei, including the anatomical planes.

3.2.4 Landmark placement

Before the landmarks were selected, the observers were given a brief introduction on how to place the landmarks for measuring the angles. The measurements for all conventional radiographs and the 3D models were performed by all observers. After a minimum of one week, the observers repeated all the measurements.

2D measurements

The landmarks placed for the 2D measurements were performed on lateral radiographs. The observers had to determine the BA and CAG on these images. To measure these angles, the observers first had to place a total of four landmarks. The first landmark was the most superior point of the processus anterior, followed by the sinus tarsi, most superior point of the ptc and most superior point of the calcaneal tuberosity. An example of the selected points in the GUI can be seen in Figure 22.

For the 2D measurements, a Python script was implemented in MeVisLab to calculate the angles. The BA was calculated by first creating two 2D vectors between landmark point 0 and 2 and between 2 and 3, after which the 2D dotproduct (equation 2) of these vectors were calculated. Thereafter, the magnitude of both lines was calculated with equation 7. After calculating the magnitude, the angle α was calculated by dividing the dotproduct with the multiplication of the magnitude of both lines. BA (β) was then calculated by subtracting angle α from 180°. For the CAG two vectors were created between point 0 and 1 and between 1 and 2. Just like BA, the same calculations were performed. However, the last step of subtracting the angle from 180 degrees was not necessary for the calculation of the CAG(γ). All the angles, including the vectors and landmarks, can be seen in figure 22.

$$|\vec{v}| = \sqrt{a1^2 + a2^2} \tag{7}$$

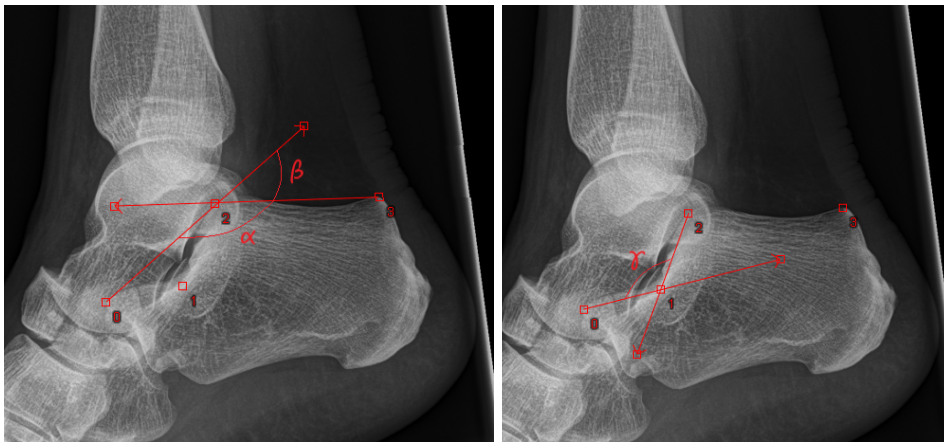

Figure 22: Selected landmarks and corresponding vectors to calculate Böhler's angle (β, left) and Critical angle of Gissane (γ, right) on conventional lateral radiographs.

3D measurements

For the 3D measurements, the landmarks were placed on 3D models of the calcaneus. The observers determined BA and the CAG, which were calculated using the same four structures as described in the 2D measurements. However, when selecting the landmarks, the observers were instructed to select the landmarks in the middle of the structures, as can be seen in Figure 23. The observers were able to rotate and translate the model in the GUI to view the selected points during the measurements. In addition, the observers were also able to show and remove the anatomical planes for better understanding of the orientation of the model.

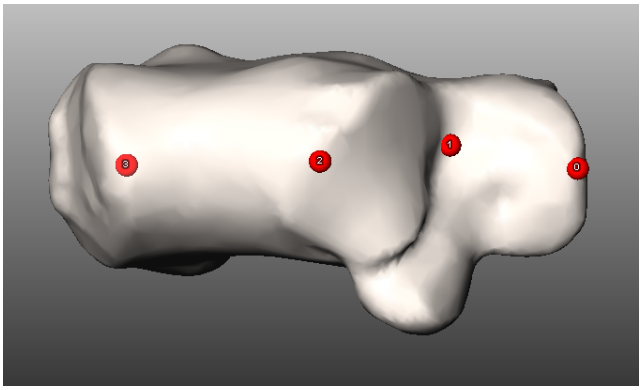

Figure 23: Example of selected landmarks in the middle of the processus anterior, sinus tarsi, ptc and calcaneal tuberosity.

For the measurement of BA and the CAG it is described in the literature that the most superior point of the anterior process, ptc and calcaneus tuberosity and the most inferior point of the sinus tarsi should be used[8]. The most superior and most inferior points were determined from the lateral view of the image because with this view, the degree of depression and displacement of the subtalar joint can be measured. Placing the landmarks precisely on the most superior or inferior point based on the lateral view is sensitive for mistakes. For this reason, an automated correction Python script was used to correct the placed landmarks. This

script moved the landmarks placed in the center of the structure to the most superior or inferior point of the selected structure. These replaced points were calculated based on the direction of normal vector of the predefined axial plane (blue) and a predefined region of interest (ROI, red boxes) around the selected landmark (Figure 24). The direction of the normal vector for the most inferior point of the sinus tarsi was rotated 180°, since here the most inferior part had to be defined. For the landmarks at which the most superior point was determined, the ROI was defined as a box around the selected landmark with a size of x = 24 mm, y = 10 mm and z = 24 mm. For the most inferior point, the box had a size of x = 8 mm, y = 5 mm z = 5 mm. The repositioning of the landmarks could only take place within the area of the ROI boxes.

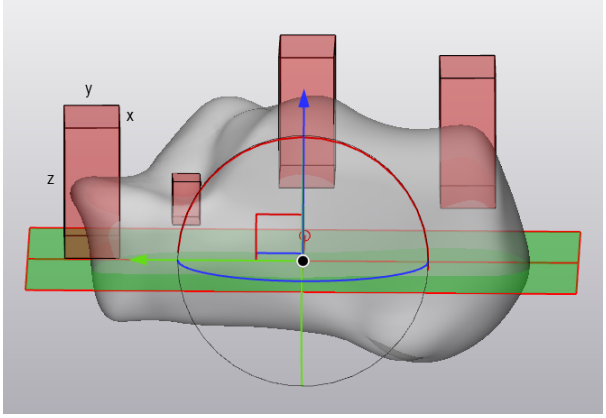

Figure 24: Lateral view of a 3D calcaneal model including the Region of interests, axial plane and normal vector of the axial plane.

The corrected points were used to calculate the angles. As with the 2D measurements, the dotproduct and magnitude were used for the calculation. However, instead of the 2D dotproduct, the 3D dotproduct was used as stated in Equation 2. The equation for the magnitude was also slightly different because a 3D vector is written as: a = (a1, a2, a3) instead of the 2D vector: a = (a1, a2). Equation 8 shows the formula to calculate the 3D magnitude of a vector.

$$|\vec{v}| = \sqrt{a1^2 + a2^2 + a3^2} \tag{8}$$

BA and the CAG indicate the degree of depression of the calcaneus, measured in lateral view. If the measurements were performed in 3D with the location of the corrected landmarks, the measured angles may give a distorted value of the depression of the calcaneus. To calculate BA and the CAG on a lateral view, the landmarks were projected onto the predefined lateral plane. To project the landmarks on the lateral plane, orthogonal projection was implemented in the Python script for measuring the angles. An example of orthogonal projection is shown in figure 25. In this example, the lateral plane is indicated by W and the selected landmark by x. Based on orthogonal projection, landmark x is projected on the plane as point x_w. The line between x and x_w is always perpendicular to the plane. This means that x_w is the closest point on the plane relative to point x. This process is repeated for all landmarks, so that every landmark in a 3D environment is projected on a 2D lateral plane. Resulting, that the measurements are performed in 2D in a 3D environment. The distance ratio between the landmarks in 3D and on the sagittal plane remains the same because x and x_w is always perpendicular to the plane.

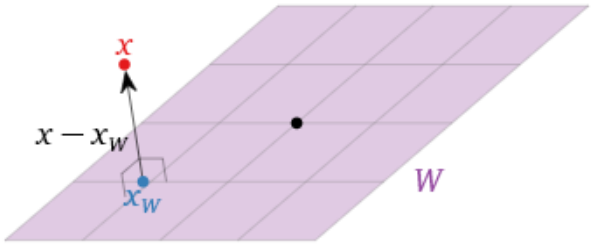

Figure 25: Example of orthogonal projection[53].

3.3 Statistical analysis

3.3.1 Intra-class correlation coefficient

Morphological measurements must be reliable and accurate, as discussed in chapter 1. For this reason, the inter-observer and intra-observer reliability for measuring BA and the CAG were calculated on both the 2D lateral radiographs and 3D models of the calcaneus. For measuring the reliability, the intra-class correlation coefficient (ICC) was calculated. The ICC score for the inter-observer reliability was calculated assuming a two-way mixed model with measures of consistency and a confidence interval of 95%[54][55]. The ICC score for the intra-observer reliability was calculated assuming a One-way random model and a confidence interval of 95%[55]. The ICC can be interpreted as follows: 0.00-0.20 slight agreement (this occurs when the observers' measurements are almost arbitrary). 0.21-0.40 fair agreement, 0.41-0.60 moderate agreement, 0.61-0.80 substantial agreement, and 0.81-1.00 almost perfect agreement [56]. The measurements were performed using IBM SPSS Statistics for Windows, version 25 (IBM Corp., Armonk, N.Y., USA).

3.3.2 Consensus given a maximum allowed discrepancy

Since the ICC does not indicate the absolute difference between the observers' measurements, it was determined how often the observers achieved consensus in measuring the BA and CAG, given an allowable discrepancy between the measurements. The difference between the measurements was determined for both the 2D and 3D measurements. The proportion of measurements for which the difference between the two measurements were at or below a certain value were determined. The difference between the measurements was then called the maximum discrepancy. For 5°, 10°, 20°, 30°, 50°and 70°, the frequency of consensus at a maximum allowable discrepancy was calculated. Because a single outlier could affect the consensus between the observers, the Bland & Altman plot was used to determine the 95% limits of agreement. The limits of agreement provides insight about the amount of 'random' measurement that may have influenced the rating[55]. IBM SPSS Statistics for Windows, version 25 (IBM Corp., Armonk, N.Y., USA) was used to determine the Limits Of Agreement.

3.3.3 Morphological parameters

For both the 2D and 3D measured BA and CAG, the mean value and standard deviation were calculated. An independent sampling t-test was performed to analyze whether there was a significant difference between the 2D and 3D measurements. The analysis was performed using IBM SPSS Statistics for Windows, version 25 (IBM Corp., Armonk, N.Y., USA).

4 Results

During the set-up of the images for the first method to determine the orientation, it soon became apparent that it would be time-consuming and difficult for the observers to place the landmarks on the correct position on the sustentaculum tali for creating the anatomical planes. In addition, there were too many calcanei where the anatomical planes did not correspond sufficiently with the desired anatomical planes. For this reason, this method will no longer be used in this Thesis. The following results were based on the second method of determining the anatomical planes based on the SSM

2D Measurements

When analyzing the measurements, the lowest inter-observer ICC of the 2D BA measurements was observed for the non-fractured population. The scores for the fractured and reconstructed population were slightly higher compared with the non-fractured population. For the non-fractured population, the inter-observer ICC was interpreted as a substantial agreement for both measurements. For both the fractured and reconstructed population, the inter-observer ICC was interpreted as an almost perfect agreement. The intra-observer ICC of the 2D BA measurements ranged between 0.70 and 0.96 (Table 1).

Table 1: Intra-class correlation coefficients for 2D böhler's angle measurements.

böhler's angle Non-fractured	**First Measurement**	**Second Measurement**	**böhler's angle Fractured**	**First Measurement**	**Second Measurement**	**böhler's angle Reconstructed**	**First Measurement**	**Second Measurement**
Inter-observer ICC	0.79, 95% CI (0.68-0.88)	0.75, 95% CI (0.63-0.85)	Inter-observer ICC	0.83, 95% CI (0.73-0.90)	0.84, 95% CI (0.75-0.91)	Inter-observer ICC	0.83, 95% CI (0.73-0.90)	0.86, 95% CI (0.78-0.92)
Intra-observer ICC			Intra-observer ICC			Intra-observer ICC		
Observer 1	0.92, 95% CI (0.85-0.96)		Observer 1	0.93, 95% CI (0.88-0.96)		Observer 1	0.90, 95% CI (0.82-0.95)	
Observer 2	0.76, 95% CI (0.59-0.86)		Observer 2	0.70, 95% CI (0.50-0.83)		Observer 2	0.88, 95% CI (0.79-0.93)	
Observer 3	0.83, 95% CI (0.69-0.90)		Observer 3	0.96, 95% CI (0.77-0.93)		Observer 3	0.89, 95% CI (0.81-0.94)	

The inter-observer ICC of the 2D CAG measurements were all scored as moderate agreement (range between 0.40-0.60), except the second measurement of the non-fractured calcanei population, which had a slightly higher ICC of 0.62. The intra-observer ICC for the 2D CAG varied a lot between the observers and between the three calcanei populations. The lowest intra-observer ICC was obtained for the fractured (range between 0.22-0.88) and reconstructed population (range between 0.38-0.62). For the non-fractured population, the intra-observer ICC ranged between 0.75 and 0.81 (Table 2).

Table 2: Intra-class correlation coefficients for 2D Critical angle of Gissane measurements.

Gissane's Non-fractured	**First Measurement**	**Second Measurement**	**Gissane's angle Fractured**	**First Measurement**	**Second Measurement**	**Gissane's angle Reconstructed**	**First Measurement**	**Second Measurement**
Inter-observer ICC	0.59, 95% CI (0.41-0.74)	0.62, 95% CI (0.45-0.76)	Inter-observer ICC	0.41, 95% CI (0.22-0.60)	0.46, 95% CI (0.26-0.64)	Inter-observer ICC	0.52, 95% CI (0.33-0.68)	0.52, 95% CI (0.33-0.68)
Intra-observer ICC			Intra-observer ICC			Intra-observer ICC		
Observer 1	0.75, 95% CI (0.58-0.86)		Observer 1	0.88, 95% CI (0.79-0.94)		Observer 1	0.62, 95% CI (0.39-0.78)	
Observer 2	0.81, 95% CI (0.66-0.89)		Observer 2	0.22, 95% CI (0.00-0.50)		Observer 2	0.54, 95% CI (0.28-0.73)	
Observer 3	0.79, 95% CI (0.64-0.89)		Observer 3	0.47, 95% CI (0.19-0.68)		Observer 3	0.38, 95% CI (0.08-0.62)	

Since the ICC does not indicate the absolute difference between the observers' measurements, it was calculated at what frequency the observers reached consensus in measuring the BA and CAG, given a maximum allowable discrepancy. For a maximum allowed discrepancy of 5°, the frequency of consensus was below 80% and 40% for the BA and CAG, respectively. For an allowed discrepancy of 10°, only a frequency of consensus above 80% was achieved for the non-fractured calcanei population in measurement of the BA (Table 3, Figure 26). The outliers determined based on the Limits Of Agreement, which may have influenced the measurements of consensus between the observers, can be seen in Table 3.

Table 3: Frequency of consensus for maximum allowable discrepancy for the 2D BA and CAG measurements, including the number of outliers based on the Limits Of Agreement.

Maximum allowable discrepancy	**Frequency of consensus**					
	Non-fractured		**Fractured**		**Reconstructed**	
	First measurement	**Second measurement**	**First measurement**	**Second measurement**	**First measurement**	**Second measurement**
böhler's angle						
5°	75% (30)	75% (30)	28% (11)	44% (17)	43% (17)	45% (18)
10°	93% (37)	95% (38)	72% (28)	69% (27)	80% (32)	73% (29)
20°	100% (40)	100% (40)	85% (33)	87% (34)	98% (39)	100% (40)
30°	100% (40)	100% (40)	95% (37)	95% (37)	100% (40)	100% (40)
50°	100% (40)	100% (40)	97% (38)	97% (38)	100% (40)	100% (40)
70°	100% (40)	100% (40)	100% (39)	100% (39)	100% (40)	100% (40)
Outliers	2	2	2	2	3	1
Gissane's angle						
5°	23% (9)	38% (15)	15% (6)	13% (5)	13% (5)	28% (11)
10°	65% (26)	75% (30)	44% (17)	38% (15)	50% (20)	55% (22)
20°	93% (37)	100% (40)	77% (30)	69% (27)	83% (33)	88% (35)
30°	100% (40)	100% (40)	87% (34)	82% (32)	93% (37)	100% (40)
50°	100% (40)	100% (40)	95% (37)	97% (38)	100% (40)	100% (40)
70°	100% (40)	100% (40)	100% (39)	100% (39)	100% (40)	100% (40)
Outliers	4	1	3	3	3	1

(a) böhler's angle 2D

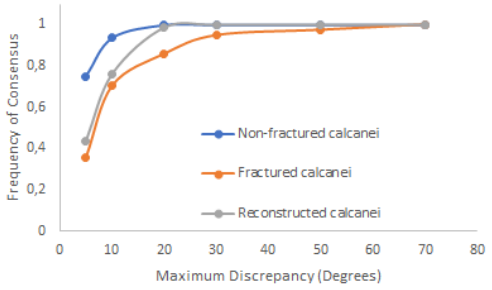

(b) Critical angle of Gissane 2D

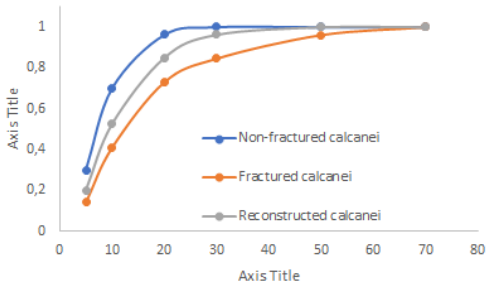

Figure 26: The frequency of Consensus given an allowable discrepancy for the 2D measurements of the BA en CAG between the observers.

3D Measurements

Comparing the ICC of the 2D BA measurements with the 3D BA measurements shows an improvement, for all measurements, of both the inter- and intra-observer ICC. The lowest ICC was obtained for the intra-observer reconstructed calcanei population, with a 0.97. In several cases, the ICC was even 1.00, indicating a perfect agreement (Table 4).

Table 4: Intra-class correlation coefficients for 3D böhler's angle measurements.

böhler's Non-fractured	**First Measurement**	**Second Measurement**	**böhler's angle Fractured**	**First Measurement**	**Second Measurement**	**böhler's angle Reconstructed**	**First Measurement**	**Second Measurement**
Inter-observer ICC	1.00, 95% CI (0.99-1.00)	1.00, 95% CI (1.00-1.00)	Inter-observer ICC	0.99, 95% CI (0.98-0.99)	0.99, 95% CI (0.98-0.99)	Inter-observer ICC	0.99, 95% CI (0.99-1.00)	0.98, 95% CI (0.97-0.99)
Intra-observer ICC			Intra-observer ICC			Intra-observer ICC		
Observer 1	1.00, 95% CI (1.00-1.00)		Observer 1	0.99, 95% CI (0.98-0.99)		Observer 1	0.97, 95% CI (0.95-0.99)	
Observer 2	1.00, 95% CI (1.00-1.00)		Observer 2	0.99, 95% CI (0.93-0.99)		Observer 2	0.99, 95% CI (0.99-1.00)	
Observer 3	0.99, 95% CI (0.99-1.00)		Observer 3	0.98, 95% CI (0.97-0.99)		Observer 3	0.99, 95% CI (0.99-1.00)	

The 3D CAG measurements also showed an improvement of all the ICC compared with the 2D CAG measurements. For the non-fractured and reconstructed population, all the ICC were above 0.90. The inter- and intra- observer ICC of the fractured population ranged from 0.89 to 0.96 and 0.87 to 0.95, respectively (Table 5).

Table 5: Intra-class correlation coefficients for 3D Critical angle of Gissane measurements.

Gissane's Non-fractured	**First Measurement**	**Second Measurement**	**Gissane's angle Fractured**	**First Measurement**	**Second Measurement**	**Gissane's angle Reconstructed**	**First Measurement**	**Second Measurement**
Inter-observer ICC	0.94, 95% CI (0.97-0.97)	0.92, 95% CI (0.87-0.96)	Inter-observer ICC	0.96, 95% CI (0.93-0.98)	0.89, 95% CI (0.82-0.94)	Inter-observer ICC	0.95, 95% CI (0.91-0.97)	0.95, 95% CI (0.91-0.97)
Intra-observer ICC			Intra-observer ICC			Intra-observer ICC		
Observer 1	0.94, 95% CI (0.88-0.97)		Observer 1	0.87, 95% CI (0.77-0.93)		Observer 1	0.92, 95% CI (0.85-0.96)	
Observer 2	0.95, 95% CI (0.91-0.97)		Observer 2	0.87, 95% CI (0.76-0.93)		Observer 2	0.94, 95% CI (0.89-0.97)	
Observer 3	0.91, 95% CI (0.83-0.95)		Observer 3	0.95, 95% CI (0.91-0.97)		Observer 3	0.96, 95% CI (0.93-0.98)	

For the 3D measurements, also the frequency of consensus between the observers was determined. With all measurements, the observers achieved more often consensus with a lower allowable discrepancy compared with the 2D measurements. For the BA non-fractured population, the frequency of consensus was 100% given an allowable discrepancy of 5°. For an allowable discrepancy of 10°, a consensus of 100% was achieved for fractured and reconstructed BA. However, at an allowable discrepancy of 5°, the of both populations was above 85%. For the CAG, the allowable discrepancy had to be set at 10°, 30°and 20°, to achieve 100% consensus between the observers, for the non-fractured, fractured and reconstructed population, respectively (Table 6, Figure 27).

Table 6: Frequency of consensus for maximum allowable discrepancy for the 3D BA and CAG measurements, including the number of outliers based on the Limits Of Agreement.

Maximum allowable discrepancy	**Frequency of consensus**					
	Non-fractured		**Fractured**		**Reconstructed**	
	First measurement	**Second measurement**	**First measurement**	**Second measurement**	**First measurement**	**Second measurement**
böhler's angle						
5°	100% (40)	100% (40)	87% (34)	87% (34)	100% (40)	93% (37)
10°	100% (40)	100% (40)	100% (39)	100% (39)	100% (40)	98% (39)
20°	100% (40)	100% (40)	100% (39)	100% (39)	100% (40)	100% (40)
30°	100% (40)	100% (40)	100% (38)	100% (39)	100% (40)	100% (40)
50°	100% (40)	100% (40)	100% (39)	100% (39)	100% (40)	100% (40)
70°	100% (40)	100% (40)	100% (39)	100% (39)	100% (40)	100% (40)
Outliers	3	2	3	1	2	2
Gissane's angle						
5°	95% (38)	83% (33)	69% (27)	38% (15)	68% (27)	78% (31)
10°	100% (40)	100% (40)	90% (35)	72% (28)	95% (38)	95% (38)
20°	100% (40)	100% (40)	100% (39)	92% (36)	100% (40)	100% (40)
30°	100% (40)	100% (40)	100% (39)	100% (39)	100% (40)	100% (40)
50°	100% (40)	100% (40)	100% (39)	100% (39)	100% (40)	100% (40)
70°	100% (40)	100% (40)	100% (39)	100% (39)	100% (40)	100% (40)
Outliers	2	3	1	3	1	2

(a) böhler's angle 3D

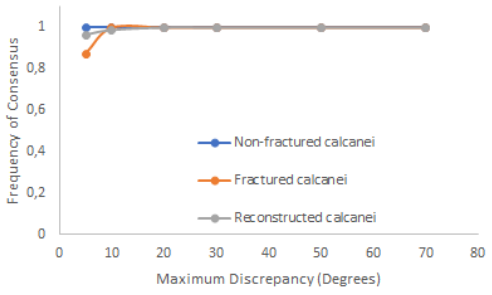

(b) Critical angle of Gissane 3D

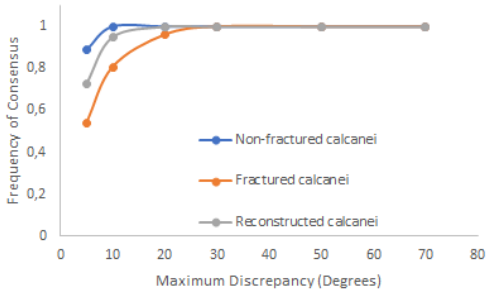

Figure 27: The frequency of Consensus given an allowable discrepancy for the 3D measurements of the BA en CAG between the observers.

Morphological parameters

For both the 2D and 3D measurements of the BA and CAG, the mean values of all populations can be seen in table 7. In addition, a significant difference between 2D and 3D measurements was found for the non-fractured and fractured calcanei population. For the reconstructed population, there was not a significant difference between the 2D and 3D measured BA and CAG.

Table 7: Morphological parameters of 2D and 3D measurements of the BA and CAG

2D böhler's angle	**Mean**	**SD**	**Min**	**Max**	**3D böhler's angle**	**Mean**	**SD**	**Min**	**Max**	**p-value**
Non-fractured	31.47	5.84	16.64	44.1	Non-fractured	29.94	5.08	18.1	42.72	0.002
Fractured	3.97	18.35	-48.98	42.8	Fractured	14.39	14.70	-45.17	38.58	0.000
Reconstructed	24.19	10.55	-8.58	62.08	Reconstructed	25.54	9.99	2.36	51.92	0.151
2D Gissane's angle	**Mean**	**SD**	**Min**	**Max**	**3D Gissane's angle**	**Mean**	**SD**	**Min**	**Max**	**p-value**
Non-fractured	123.33	7.64	102.49	147.25	Non-fractured	128.15	6.15	112.87	147.36	0.000
Fractured	125.11	14.13	78.62	165.07	Fractured	117.59	15.59	72.53	144.05	0.000
Reconstructed	127.64	9.99	96.62	163.83	Reconstructed	127.10	12.17	96.22	151.81	0.597

Discussie start vaak met korte samenvatting van studie alsmede belangrijkste resultaten. Ontwikkelen van dit en dat en experiment met dit en dat en resultaten zus en zo.

5 Discussion

The aim of this thesis was to develop a novel method to perform morphological measurements based on 3D models of the calcaneus obtained from CT-scans. The morphological measurements were BA and the CAG, which were measured on 40 non-fractured, 39 fractured and 40 reconstructed calcanei populations. For these populations, the ICC for inter- and intra-observer reliability was determined. In addition, the frequency of consensus given an allowable discrepancy was calculated. All measurements and statistical analyzes were also performed on conventional 2D X-rays so that the results could be compared. Before the measurements could be performed on the 3D models, 3D models had to be created based on the CT-scans. Thereafter, an SSM model was created based on the non-fractured calcanei population. The orientation of this SSM model was then used as the standard orientation, and all the other 3D calcanei models were aligned on top of this SSM model. This resulted that all models were position at the same location in the same world coordinate system. After this process, a total of three observers performed the 2D and 3D measurements twice in a specially designed GUI.

For the 2D measurements, a good intra-class correlations of the BA was determined, at which most ICC were above the 0.80, indicating a good agreement. The intra-class correlation for the CAG, showed moderate agreement for all inter-observer measurements. The intra-observer measurements, showed large discrepancy between the observers. The lowest (range 0.22-0.88) and highest (range 0.5-0.81) ICC were seen for the fractured and non-fractured population, respectively. To indicate the absolute difference between these discrepancies, it was determined how often the three observers truly agreed with each other when measuring the BA and CAG. Even with an allowed discrepancy of 10°between the observers, they lacked to achieve consensus in more than 20% of the measurements, except for measuring the BA on the non-fractured calcanei population. To achieve a consensus of 80% between the observers, an allowed discrepancy of at least 20°was needed for most measurements. For measuring the CAG on the fractured and reconstructed population, even an allowed discrepancy of 30°was needed.

3D BA and CAG measurements showed an improvement for both the inter- and intra-observer ICC. For the BA, the lowest ICC was obtained for the intra-observer reconstructed calcanei population, with a 0.97. The rest of the BA ICC were close or equal to 1.00, which indicate a perfect agreement. The CAG for the inter- and intra-observer ICC ranged from 0.89 to 0.92 and 0.87 to 0.96, respectively. To achieve 80% consensus for the BA among the observers, only an allowable discrepancy of 5°was needed. For the CAG, 80% of consensus was achieved with 5°, 20°and 10°for the non-fractured, fractured and reconstructed calcanei population, respectively.

5.1 Previously reported results

2D measurements

Comparing the 2D inter-observer ICC BA measurements with previous reports, shows similar results for the non-fractured calcanei population, ranging between 0.63 and 0.94[26][42][43][57]. The inter-observer ICC for CAG measurements, has been reported a single time with an ICC of 0.40[43], which was 0.20 lower than reported in this thesis. To our knowledge, there is no data available in previously reported studies about the intra-observer ICC for BA and CAG measurements based on the non-fractured calcanei population.

For the fractured and reconstructed population, the 2D inter- and intra-observer reliability has been reported as limited in multiple occasions, where a large discrepancy can be seen. These studies showed comparable inter-observer ICC for BA and CAG measurements [44][43][45][46][58][59][60]. However, the inter-observer ICC for BA in this thesis, scored relatively high compared with the previously reported studies. The intra-observer ICC for the fractured and reconstructed population was similar to the previously reported studies [45][46][59][60].

Jesse et al.[46], also reported the frequency of consensus between the observers for the

2D BA and CAG measurements. For the fractured and reconstructed calcanei population, they reported that even with a given discrepancy of 20°, the observer achieved consensus in 60% and 40% for the BA and CAG, respectively. In this thesis, however, the frequency of consensus, with an allowable discrepancy of 20°was reported 80% and 70% for the BA and CAG, respectively.

In the literature, it is stated that the normal values for the BA and CAG range from 20°to 40°and 120°to 145°, respectively[8]. The mean values for the 2D non-fractured calcanei population in this thesis fall within the normal values. As described previously, deviations from these angles indicate a possible fracture of the calcaneus. The mean fractured BA population was measured below normal range of non-fractured calcanei, and thus would be indicated as fractured. However, the mean fractured CAG was almost equal to the non-fractured population, while the literature states that the angle should become larger in most cases due to depression of the ptc[8]. After reconstruction of the calcanei, the mean BA and CAG were both within the normal range of the angles.

3D measurements

As reported previously, a few studies have developed a novel method to perform morphological measurements based on 3D models of the calcaneus. In three studies, the ICC was measured for the BA and/or CAG based on non-fractured 3D models of the calcaneus. To our knowledge, there are no studies that have reported the ICC for fractured or reconstructed calcanei populations. Qiang et al.[29] performed the measurements based on manual landmark selection, while Irwamsyah et al.[33] performed the measurements based on curvature measurements on 3D models of the calcaneus. Qiang et al.[29] and Irwamsyah et al.[33], reported an intra-observer ICC of 0.95 and 0.74 for the BA, respectively. For the CAG, the intra-observer ICC was stated as 0.96 and 0.13, respectively. The inter-observer ICC was only reported by Qiang et al.[29], with 0.91 for the BA and 0.89 for the CAG. A different approach of measuring the CAG was developed by Schmutz et al.[34] based on manual landmark selection, which used the lateral, central and medial anatomy of the ptc and sinus tarsi to measure the CAG. The calculated intra-observer ICC ranged from 0.89 to 0.93, 0.93 to 0.93 and 0.63 to 0.62 for the lateral, center and medial CAG measurement, respectively. However, the measurements were only repeated five times by two raters, which indicates that the ICC results are not reliable because at least 51 sample are required for a reliable measurement with two observers[51]. Comparison of the results of this thesis with previously reported BA and CAG ICC from non-fractured calcanei population shows an improvement compared to the results of Irwamsyah et al.[33]. However, they only measured the intra-observer ICC and not the inter-observer ICC. The results of Qiang et al.[29], were comparable with the results in this thesis. The frequency of consensus given an allowable discrepancy has not been reported yet for 3D measurements on 3D models of the calcaneus.

Morphological parameters

The results in this thesis showed that there were significant differences between the 2D and 3D measurement of the BA and CAG for the non-fractured and fractured population. This means that the mean morphological 3D measurements cannot be compared with the 2D mean measurements. Because of this, it cannot be stated whether the mean 3D morphological measurements were within the normal range of non-fractured calcanei. The previously reported studies reported mean morphological measurements for non-fractured and reconstructed calcanei. The mean 3D BA based on 3D models of non-fractured calcanei ranged from 33.4° to 37°. The CAG was reported from 105.1°to 131°[29][30][32][33][34]. In this thesis, the mean 3D BA and CAG were measured as 29.94°and 128.15°, respectively. The BA was reported smaller and the CAG equal in comparison with the other reports. Qiang et al.[31], reported the mean BA and CAG for the reconstructed calcanei population with 28.85 and 131.35, respectively. for this thesis, the mean BA and CAG were reported as 25.54 and 127.10, respectively.

Dominique et al.[61], developed a novel method to measure the depression of the ptc based

on 3D models of the calcaneus. They first had to indicate the surface of the posterior facet. Thereafter, an angle was created between the normal vector of this surface and the normal axial axis of the calcaneus. The results showed that this technique was reliable and thus safe to use in clinical practice.

5.2 Limitations

Segmentation

There were a few limitations when creating the 3D models of the calcaneus. In this study, retrospective data was used between 2006 and 2021. Most of the images were made in Erasmus MC, but there were also imported images from other hospitals, as a result, the properties of the CT-scans were different. Due to this, the quality of the images was poor in some cases. This resulted, that some images were difficult to segment, which was mainly due to different slice thicknesses, artifacts and HU of the voxels. The difference was especially noticeable between the three different populations: non-fractured, fractured and reconstructed calcanei. If a standardized protocol was used for making the CT-scans, the segmentations process would have been performed in a more equivalent manner between the different scans.

Due to the poor quality of CT-scans, it sometimes occurred that imported structures which were used to perform the measurement had to be manually segmented. Especially for the fractured calcanei population, this often occurred, which may have caused minor error in the results.

Orientation & registration

The registration process of the models on the SSM were validated based on visual inspection. Another way to validate the registrations is through quantitative validation. For example, landmark-based validation could have been used, in which certain anatomical structures are used to determine the accuracy of the registration.[62]. The absolute median deviation between the models could then be examined based on the Euclidean distance between the landmarks of the anatomical structures.

The last important point of attention for the orientation/registration is the fact that the same anatomical planes were used for all calcanei and that the most superior and inferior landmarks were determined by the direction of normal vector of the predefined axial plane. The influence of the anatomical planes at different angles has not been investigated. There may be a significant difference between measured angles, if different 'standard' anatomical planes were used (e.g. 5°, 10°, 20°, 40°rotation in various directions). Siebe et al.[48] investigated the effect of the obliquity of the radiation beam based on 2D lateral radiographs. This showed that there was no significant difference between the different angles. However, the question remains whether this is also the case when measuring morphological measurements based on 3D models.

Landmark placement

When placing landmarks on the 3D models, there were also a few limitations to the novel developed method. As described previously, the algorithm searches around the selected landmark for the most superior or inferior point, depending on the selected structure, and corrects the placed landmark to the actual most superior or inferior point. The algorithm uses a ROI with a certain size. However, if an observer does not place the landmark in the center of the structure or if the landmark is placed too close to a fracture (this only affected the landmarks placed on the sinus tarsi) the algorithm may not place the landmark at the actual most superior or inferior point. Figure 28 shows a few examples of a few errors that can occur when using the algorithm. In red(0-3) and purple(4-7) the first placed and corrected landmarks are indicated, respectively.

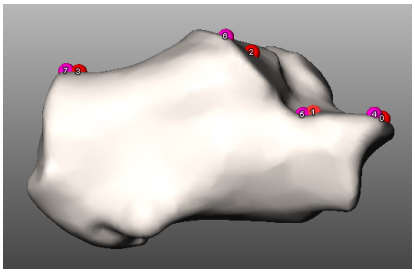

(a) Landmark to far from the ptc

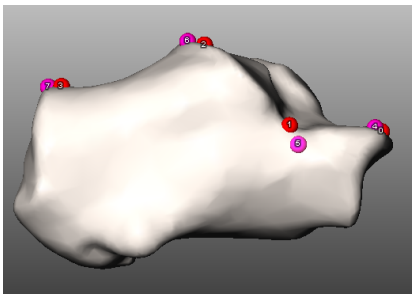

(b) Sinus tarsi lateral wall

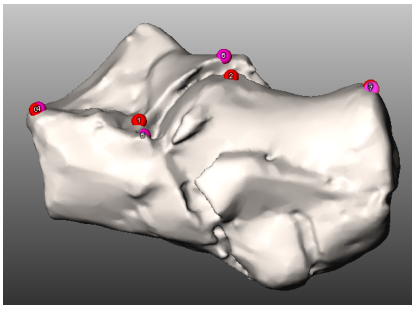

(c) Fracture through Sinus tarsi

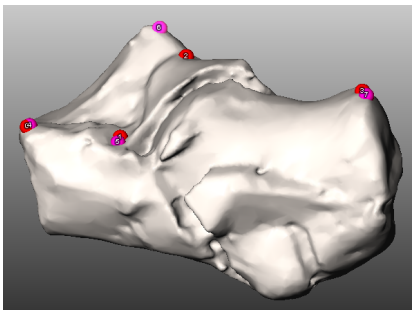

(d) landmark to close to the sustentaculum tali

Figure 28: Figure a: landmark 2 is placed too much anterior, resulting that the actual most superior point of the ptc is not within the ROI. Figure b: landmark 1 is placed too close to the lateral wall, resulting that the algorithm places the corrected landmark on the lateral wall, instead of the sinus tarsi. Figure c: landmark 1 is placed too close to the fracture line, resulting that the corrected landmark is placed in the fracture. Figure d: landmark 2 is placed too far medially, resulting that the corrected landmark is placed on the sustentaculum tali.

Due to the structure of the calcaneus and the pattern in which the calcaneus is depressed after a fracture, it appears that the algorithm work best to reproduce the landmarks on the anterior process, ptc and calcaneal tuberosity. This has to do with the fact that for these landmarks, the most superior point is detected. However, correcting the landmark on the sinus tarsi is more challenging. As can be seen in figure 28c a fracture causes the algorithm to define the most inferior point of the sinus tarsi within the fracture. In addition, the sinus tarsi was interpreted in different ways by the observers. Figure 29a and figure 29b shows different placed landmarks by the observers on a 2D lateral radiograph and a 3D model of the same calcaneus. The fact that the observers could not agree on the location of the sinus tarsi on a good assessable image raises questions. The poorer reliability of the CAG compared to the BA is probably related to the landmark placement of the sinus tarsi, especially for the fractured population. The question is therefore whether measuring the CAG on the fractured calcanei population is reliable. It also appears from the literature that the CAG is included much less often because it does not provide additional essential information about the degree of depression and displacement of the subtalar joint of the calcaneus. measuring the BA already gives enough information regarding the degree of depression and displacement of the subtalar joint of the calcaneus, resulting that measuring the CAG may be superfluous.

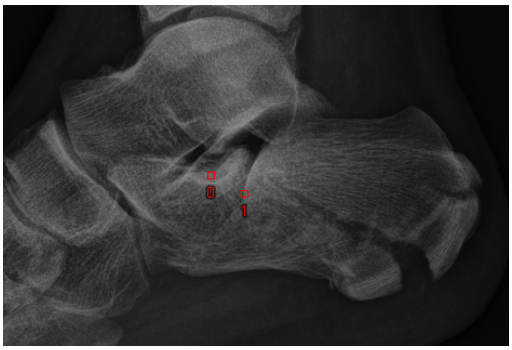

(a) to be written

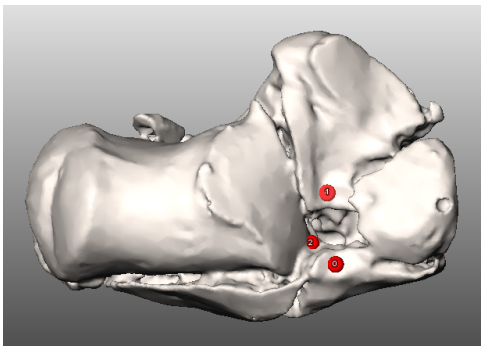

(b) to be written

Figure 29: Böhler's angle measured from different views

Validation

In this thesis, conventional radiographic measurements on the calcaneus were compared with a novel developed method to perform these measurements based on a 3D model of the calcaneus. However, the measurements on the 3D models were not validated in this thesis. To properly validate the measured angles, comparison with the conventional way is not enough, as it cannot be seen as the ground truth. The first option to validate the measured angles in 3D is to have the 3D models printed in 3D, after which the angles must be measured again in a specially designed setup. The results from the measured angles in the GUI should then be compared with the angles measured with the goniometer. A second option is to use the calcaneus of deceased patients. A CT-scan of the lower leg should be performed, after which a 3D model of the calcaneus should be created. After that, the calcaneus will have to be removed from the patient's leg. The measurements of the angles on the 3D model should be performed in the GUI, and the removed calcaneus can also be performed with a specially designed setup. Also, these results must then be compared with each other to validate the angles measured with the GUI.

5.3 Recommendation

Currently, the developed GUI can be used to measure the BA and CAG based on semi-automated landmark placement algorithm. However, this process is still time-consuming, including a few limitations as previously described. To improve the current process and to better understand the whole morphology of the calcaneus, additional functions could be implemented in the tool. First, additional morphological descriptions by mean of more landmarks could be added for better analysis of fractured and reconstructed calcanei (e.g. varus/valgus angulation, calcaneal width, calcaneal length, ect). To shorten the time before the measurements can be used, Artificial intelligence (AI) could be of great help. Especially, automated segmentation, automated 3D reconstruction and automated landmark selection could reduce the time significantly, which manually sometimes takes up to 60 minutes per calcaneus. The automated morphological measurements could also be used for guidance of further treated of patients after surgical reconstructions and patients with a malunion. With the automation of this process, a user may be able to describe bone morphology with a single click of a button. The measurements, however, can currently only be used in a special program that is not easily accessible to surgeons. To be able to use this tool by surgeons during daily clinic, it could be incorporated in, for example, the PACS system in the hospital. Lastly, the method to perform morphological measurements could also be translated towards other bones for fracture and deformity characterization and deformity correction.

We hypothesize that the additional implementations as described could be very useful for orthopedic- and trauma-surgeons and radiologists around the world, as it would save time wasted by eliminating the need to perform manual measurements of fracture and deformity

morphology. In addition, it is assumed that the measurements will be more reliable. Furthermore, this process for describing the morphology of the calcaneus can also be extrapolated to other bone structures such as the femur, tibia, radius, ulna, ect.

5.4 Conclusion

In conclusion, the 3D angle measurements on 3D models of the calcaneus are more reliable in comparison with the conventional 2D measurements. However, new studies are necessary to validate the placed landmarks, which were used to measure the angles on 3D models of the calcaneus, before this novel method could be used for diagnosis, treatment and prognosis of calcaneal fractures. If the method is validated, more landmarks could be used to describe the whole morphology of the calcaneus based on the same semi-automated landmark placement technique. However, the presented method is still time-consuming, which could possibly be solved by using AI.

References

[1] Sengodan VC, Amruth KH, and Karthikeyan. Bohler's and gissane angles in the indian population. *J Clin Imaging Sci.*, 2:77, 2012.

[2] Daftary A, Haims AH, and Baumgaertner MR. Fractures of the calcaneus: a review with emphasis on ct. *RadioGraphics.*, 25(5):1215–1226, 2005.

[3] Davis D, Seaman TJ, and Newton EJ. Calcaneus fractures. *StatPearls*, 2021.

[4] Mitchell MJ, McKinley JC, and Robinson CM. The epidemiology of calcaneal fractures. *The Foot*, 19(4):197–200, 2009.

[5] De Boer AS, Schepers T, Panneman MJ, Van Beeck EF, and Van Lieshout EM. Health care consumption and costs due to foot and ankle injuries in the netherlands. *BMC Musculoskelet Disord*, 15:128, 2014.

[6] Ko M Donaldson C Brauer CA, Manns BJ and Buckley R. An economic evaluation of operative compared with nonoperative management of displaced intra-articular calcaneal fractures. *J Bone Joint Surg Am*, 87:2741–2749, 2005.

[7] Benson E, Conroy C, Hoyt DB, Eastman AB, Pacyna S, Smith J, Kennedy F, Velky T, and Sise M. Calcaneal fractures in occupants involved in severe frontal motor vehicle crashes. *Accid Anal Prev.*, 39(4):794–9, 2007.

[8] Keener BJ and Sizensky JA. The anatomy of the calcaneus and surrounding structures. *Foot and Ankle Clinics*, 10(3):413–424, 2005.

[9] Swords MP Rammelt S, Sangeorzan BJ. Calcaneal fractures — should we or should we not operate? *IJOO*, 52(3):220–230, 2018.

[10] Anderson Robert B MD Nickisch Florian MD Banerjee Rahul MD, Saltzman Charles MD. Management of calcaneal malunion. *American Academy of Orthopaedic Surgeon*, 19(1):27–36, 2011.

[11] Tough S et al. Dooley P, Buckley R. Bilateral calcaneal fractures: Operative versus nonoperative treatment. *Foot Ankle International*, 25(2):47–52, 2004.

[12] David P Barei, FRCS, Carlo Bellabarba, and et al. Fractures of the calcaneus. *Orthopedic Clinics of North America*, 33(1):263–285, 2002.

[13] Salih Angin and İlkşan Demirbüken. Comparative kinesiology of the human body. *Ankle and foot complex*, pages 411–439, 2020.

[14] Maskill JD, Bohay DR, and Anderson JG. Calcaneus fractures: a review article. *Foot Ankle Clin.*, 10(3):463–89, 2005.

[15] White EA, Skalski MR, Matcuk GR, and et al. Intra-articular tongue-type fracture of the calcaneus: anatomy, injury patterns, and an approach to management. *Emergency Radiology*, 26(1):67–74, 2019.

[16] Gupton M, Özdemir M, and Terreberry RR. Anatomy, bony pelvis and lower limb, calcaneus. *StatPearls [Internet]*, 2021.

[17] Greiner TM and Ball KA. The calcaneocuboid joint moves with three degrees of freedom. *Foot and Ankle Research*, 1(1):039, 2008.

[18] Sammarco VJ. The talonavicular and calcaneocuboid joints: anatomy, biomechanics, and clinical management of the transverse tarsal joint. *Foot and Ankle Clinics*, 9(1):127–45, 2004.

[19] Singh AP. (2018, august 8). calcaneus anatomy and attachments. bone and spine. retrieved october 15, 2021, from https://boneandspine.com/calcaneus-anatomy-and-attachments/.

[20] Rammelt S and Zwipp H. Calcaneus fractures: facts, controversies and recent developments. *Injury.*, 35(5):443–461, 2004.

[21] Al-Ashhab ME and Elgazzar AS. Treatment for displaced sustentaculum tali fractures. *The Foot*, 35:70–74, 2018.

[22] Buckley R and Sands A. Displaced fracture of the calcaneus body. ao surgery reference. accessed at 29 september 2021, from https://surgeryreference.aofoundation.org/orthopedic-trauma/adult-trauma/calcaneous/displaced-body-fractures/definition.

[23] Brian PL and Mahraj RPM. Imaging of the calcaneus. *Foot and Ankle Clinics*, 10(3):442–461, 2005.

[24] Stefan Rammelt and Akaradech Pitakveerakul. Hindfoot injuries: How to avoid posttraumatic varus deformity? *Foot and Ankle Clinics*, 24(2):325–345, 2019.

[25] Anthony J. (2015, june). bohler's angle: How to determine presence of a calcaneus fracture. ebm consult. retrieved october 15, 2021, from https://www.ebmconsult.com/articles/bohlers-angle-calcaneus-fractures.

[26] Ma Z-J, Bai L-P, Zhang G-M, Zhang L-B, and Chen Z. Natural value of böhler's angle in normal chinese population. *Orthop Surg*, 11(6):1201–1208, 2019.

[27] Anthony J. (2015, june). critical angle of gissane: How to use in the diagnosis of a calcaneus fracture. ebm consult. retrieved october 15, 2021, from https://www.ebmconsult.com/articles/critical-angle-gissane-calcaneus-fractures.

[28] Pombo B, Ferreira AC, and Costa L. Bohler angle and the crucial angle of gissane in paediatric population. *Clin Med Insights Arthritis Musculoskelet Disord*, 12, 2019.

[29] Qiang M, Chen Y, Zhang K, and et al. Measurement of three-dimensional morphological characteristics of the calcaneus using ct image post-processing. *J Foot Ankle Res*, 19, 2014.

[30] Melinska AU, Romaszkiewicz P, Wagel J, Sasiadek M, and Iskander DR. Statistical, morphometric, anatomical shape model (atlas) of calcaneus. *PLoS ONE*, 10(8), 2015.

[31] Qiang M, Chen Y, Jia X, and et al. Post-operative radiological predictors of satisfying outcomes occurring after intra-articular calcaneal fractures: a three dimensional ct quantitative evaluation. *International Orthopaedics (SICOT)*, 41(9), 2017.

[32] Irwansyah, Lai J-Y, Essomba T, and Lee P-Y. Measurement and analysis of calcaneus morphometric parameters from computed tomography images. *Proceedings of the 2018 5th International Conference on Biomedical and Bioinformatics Engineering*, pages 82–86, 2018.

[33] Irwansyah, Lai J-Y, and Lee P-Y. A reliable method for morphological measurement of 3d calcaneus models from computed tomography images. *Biomedical Research*, 30(1):149–159, 2019.

[34] Schmutz B, Lüthi M, Schmutz-Leong YK, Shulman R, and Platt S. Morphological analysis of gissane's angle utilising a statistical shape model of the calcaneus. *Arch Orthop Trauma Surg*, 141(6):937–945, 2021.

[35] Hounsfield GN. Computed medical imaging. nobel lecture, december 8, 1979. *J Comput Assist Tomogr*, 4(5):665–74, 1980.

[36] Gurushanth K Raghavan As Gurudath S Patrick S, Birur Np. Comparison of gray values of cone-beam computed tomography with hounsfield units of multislice computed tomography: An in vitro study. *Indian J Dent Res*, 28(1):66, 2017.

[37] Türk G Kılınç CY Yeniçeri İÖ Kılınc RM, Açan AE. Evaluation of femoral head bone quality by hounsfield units: a comparison with dual-energy x-ray absorptiometry. *Sage Journals*, 2021.

[38] C Jud M Lüthi, T Gerig and T Vetter. Gaussian process morphable models. *in IEEE Transactions on Pattern Analysis and Machine Intelligence*, 40(8):1860–1873, 2018.

[39] T Albrecht T Gass O Goksel P Büchler M Kistler H Bousleiman M Reyes P C Cattin T Vetter M Lüthi, R Blanc. Statismo - a framework for pca based statistical models. *The Insight Journal*, pages 1–18, 2012.

[40] Cadima J Jolliffe IT. Principal component analysis: a review and recent developments. *Phil Trans R Soc A*, 374(2065), 2016.

[41] Zhao X Zhang L Li F, Liu S. Real-time 2-d lidar odometry based on icp. *Sensors*, 21(21):7162, 2021.

[42] Šimunović M, Nizić D, Pervan M, Radoš M, Jelić M, and Kovačević B. The physiological range of the böhler's angle in the adult croatian population. *Foot Ankle Surg*, 25(2):174–179, 2019.

[43] Barroco R dos S, Miranda BR de, Fernandes HA, and et al. Inter-rater reliability of böhler and gissane angles in different calcaneal fracture according to the essex-lopresti and sanders classifications. *Journal of the Foot Ankle*, 15(2):133–139, 2021.

[44] Labronici PJ, Faria GGP de, Pedro BM, Serra MDF de A, Pires RES, and Tamontini JL. Böhler's angle—comparison between the pre- and postoperative in displaced intra-articular calcaneal fractures. *Rev Bras Ortop (Sao Paulo)*, 54(2):156–164, 2019.

[45] T Bulut and M Gursoy. Are radiological measurements reliable methods in the postoperative follow-up of calcaneal fractures. *Nigerion journal of clinical practice*, 24(1):110–114, 2021.

[46] Jesse E Otero, Brian O Westerlind, Saran Tantavisut, Matthew D Karam, Phinit Phisitkul, Craig C Akoh, Yubo Gao, and J Lawrence Marsh. There is poor reliability of böhler's angle and the crucial angle of gissane in assessing displaced intra-articular calcaneal fractures. *Foot and Ankle Surgery*, 21(4):277–281, 2015.

[47] Gonzalez TA, Ehrlichman LK, Macaulay AA, and et al. Determining measurement error for bohler's angle and the effect of x-ray obliquity on accuracy. *Foot Ankle Specialist.*, 9(5):409–416, 2016.

[48] A Siebe De Boer, Esther MM Van Lieshout, Leonie Vellekoop, Dennis Den Hartog, Gert Jan Kleinrensink, and Michael HJ Verhofstad. The influence of radiograph obliquity on böhler's and gissane's angles in calcanei. *The Journal of Foot and Ankle Surgery*, 59(1):44–47, 2020.

[49] Arifin WN. Sample size calculator (web) [Internet]. 2022 [cited 15 March 2022]. Available from: http://wnarifin.github.io.

[50] Eliasziw M Walter SD and Donner A. Sample size and optimal designs for reliability studies. *Statistics in Medicine*, 17(1):101–110, 1998.

[51] Bonett DG. Sample size requirements for estimating intraclass correlations with desired precision. *Statist Med*, 21(9):1331–1335, 2002.

[52] von Tycowicz C Zachow S Ambellan F, Lamecker H. Statistical shape models: understanding and mastering variation in anatomy. *Rea PM, ed. Biomedical Visualisation*, 1156:67–84, 2019.

[53] Interactive Linear Algebra [Internet]. 2022 [cited 29 March 2022]. Available from: https://textbooks.math.gatech.edu/ila/projections.html Dan M, Joseph R.

[54] Fleiss JL Shrout PE. Intraclass correlations: Uses in assessing rater reliability. *Psychological Bulletin*, 86(2):420–428, 1979.

[55] Center of excellence SIGMA in mathematics & statistics support [Internet]. [cited 05 April 2022]. Available from: https://www.statstutor.ac.uk/resources/uploaded/coventryreliability.pdf.

[56] Landis J Richard and Gary G Koch. The measurement of observer agreement for categorical data. *Biometrics*, 33(1):159–74, 1977.

[57] H Willmott, J Stanton, and C Southgate. Böhler's angle – what is normal in the uninjured british population. *Foot and Ankle Surgery*, 18(3):187–189, 2012.

[58] JR Knight, EA Gross, GH Bradley, and et al. Boehler's angle and the critical angle of gissane are of limited use in diagnosing calcaneus fractures in the ed. *Am J Emerg Med*, 24(4):423–427, 2006.

[59] Sayed-Noor AS, Ågren P-H, and Wretenberg P. Interobserver reliability and intraobserver reproducibility of three radiological classification systems for intra-articular calcaneal fractures. *Foot Ankle Int*, 32(9):861–866, 2011.

[60] Ewout S Veltman, Michel PJ van den Bekerom, Job N Doornberg, Diederik O Verbeek, Stefan Rammelt, Ernst Ph Steller, and Tim Schepers. Three-dimensional computed tomography is not indicated for the classification and characterization of calcaneal fractures. *International Orthopaedics*, 45(7):1117–1120, 2014.

[61] Hoekstra H Nijs S Matricali G Misselyn D, Caeyman A. Intra- and inter-observer reliability of measurements on 3d images of the calcaneus bone. *Computer Methods in Biomechanics and Biomedical Engineering*, 24(5):579–583, 2021.

[62] Wang G zhien Liu Z, Deng X. Accuracy validation for medical image registration algorithms: a review. *Chinese Medical Sciences Journal*, 27(3):176–181, 2012.

[63] MeVisLab. Manual MeVisLab [Internet]. 2022 [cited 17 March 2022]. Available from:. https://mevislabdownloads.mevis.de/docs/current/mevislab/resources/documentation. /Publish/SDK/GettingStarted/index.html.

A Graphical user interface

Appendix A shows the design of the Graphical User Interface (GUI), which was used for 2D and 3D morphological measurements on the calcaneus. Modules in MeVisLab were connected with each other, forming a network. Two different networks were created for 2D and 3D measurements. Thereafter, a GUI was created so that the observers, who performed the measurements, could interact with these networks.

A.1 2D Module Network

The MeVisLab network used to design the GUI for the 2D measurements on the calcaneus can be seen in Figure 30. The outlines with numbers indicate different functions of the network, which will be explained in more detail.

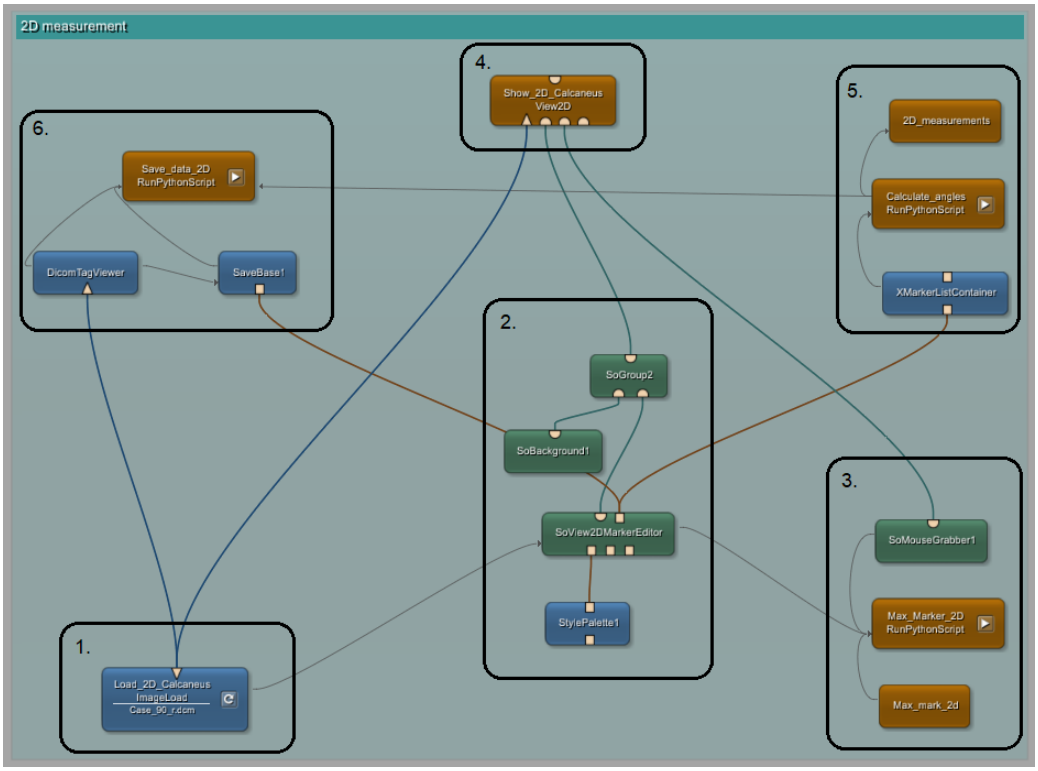

Figure 30: MeVisLab module network for 2D measurements

Number 1. is an ML model that was used to load in conventional radiographs. With this module, different types of data formats can be loaded, such as: DICOM, TIFF, PNG, JPEG, ect[63]. The function of block number 2 was to place, remove or replace landmarks. In addition, the style (e.g. size) of the placed landmark could be adjusted. In Block number 3, a Python script was implemented so that only a maximum number of landmarks could be placed. Block number 4 was a macro module to combine the previously mentioned blocks. Through this module, it was possible to interact with a loaded image in a very basic manner (e.g. select landmark)(Figure 31). In block number 5, the XMarkerListContainer module was used to extract the data of the placed landmarks. These data was subsequently used to calculate the desired angles through a python script. The last block number 6 was used to save the important data and export these as txt-files to an appropriate folder.

Figure 31: 2D image visualization from the sagittal view in MeVisLab, including selected landmarks.

A.2 3D Module Network

The module network for the 3D measurements is more extensive due to additional functions required for the network to function. In addition, extra functions were implemented so that a more user-friendly GUI environment could be created. The network can be seen in Figure 32 and the different functions will be discussed in more detail.

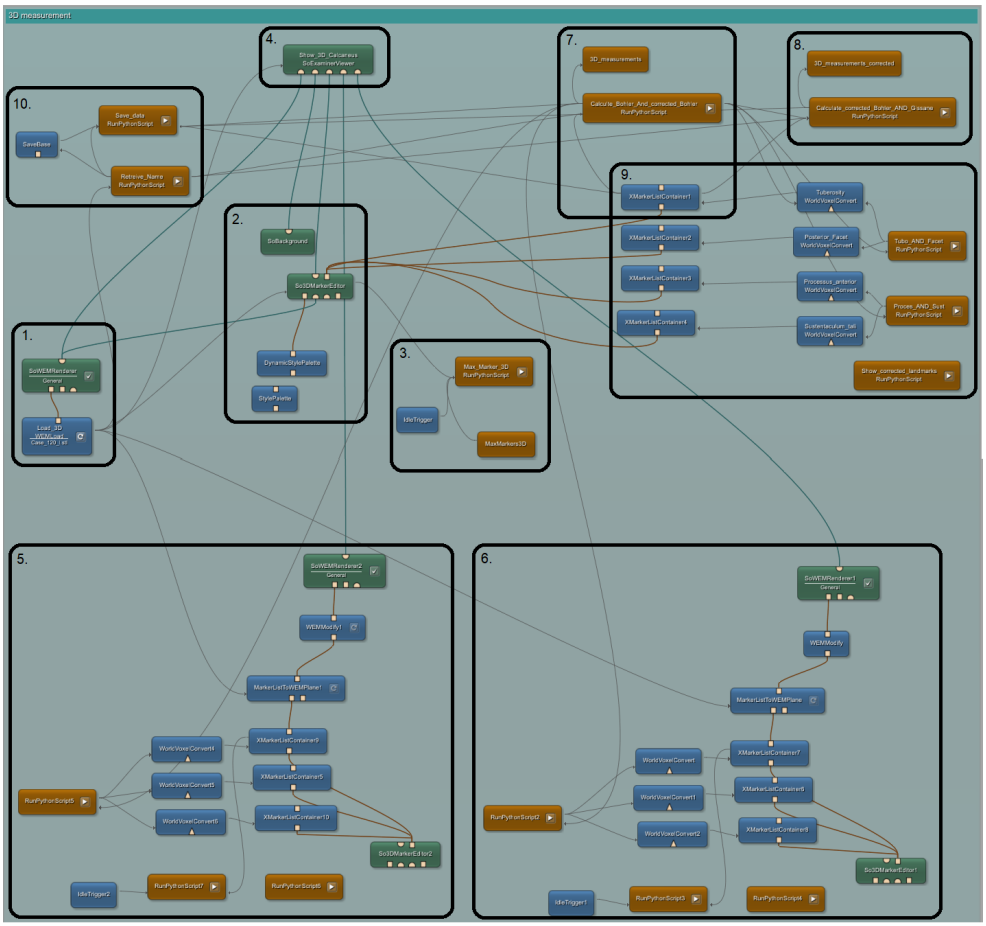

Figure 32: MeVisLab module network for 3D measurements

As with the 2D module network, block number 1 was also used to load in the data. However, only 3D mesh file formats are supported by this module, such as: *.obj, *.ply, *.stl, ect[63]. The data currently only consists out of vertices. The edges and faces still need to be rendered between the vertices to be able to display and interact with the 3D model. This was performed using the additional open inventor module. Block number 2 and 3 have the same functions as with the 2D module network. Block 2 is used for placing landmarks, and block 3 so that there is a maximum for the number of landmarks to be placed. With block number 4, the previous mentioned block were connected. This results in a small interface where 3D models can be displayed and interacted with. In this interface, the user can interact with the model in a basic way by rotating the model and placing landmarks.(Figure 33a). To clarify the position of the model in the world coordinate system, two additional functions have been added to the network. These functions can be seen in block number 5 and 6, which are used to generate an axial and sagittal plane, respectively (Figure 33b). Block 7 is used to extract import data information about the placed landmarks. In addition, the python scripts in this block used the data of the placed landmarks for calculation of the angles, but were also used to correct the landmarks placed by the observers. The angles for the corrected landmarks were then calculated in block 8. To visualize the corrected landmarks, block 9 was developed. To eventually store all data, block 10 was used to export the data as txt-files.

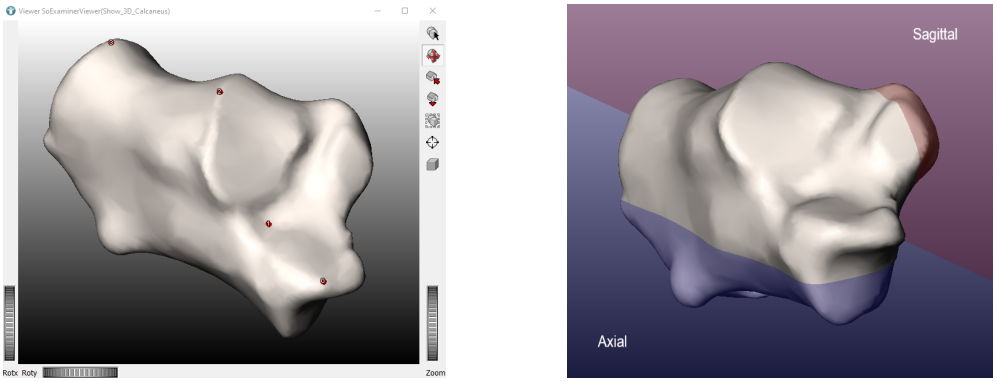

(a) Landmark placement (b) Plane visualization

Figure 33: 3D visualization in MeVisLab

A.2.1 The interface

Interaction with block number 4 as can be seen in Figure 31 & 33a was limited. These interfaces could only be used to set landmarks, or could be used to perform simple actions with the models (e.g. zooming, moving, rotation, ect). Deleting points, loading images, saving images, show information about the placed landmarks, adding and removing the planes, ect, were only possible by opening different function blocks. Most interfaces consisted of several tabs and displayed unnecessary information, making it inconvenient for the user to use these interfaces. To create an interface for the user in which only the necessary information was visual, and so that the user could perform all necessary actions for the measurements, MeVisLab implemented the possibility to develop a GUI yourself. This interface was created based on MeVisLab Definition Language (MDL), a configuration and layout language. This language is based on the architecture pattern model-view-control(MVC)[63]. For the user, a GUI was developed based on the 2D and 3D module networks.

The interfaces created had different functions. At the top of the interface, the users were able to switch between the interfaces for the 2D and 3D measurements (Figure 34 & 35). The browse button with the load button allowed the user to load in radiographs (2D measurement tab) and 3D models (3D measurement tab). How the user should interact with the images was displayed in the manual as displayed in the interfaces. When all landmarks were placed as

described in the manual, the measured angles were displayed. To show the corrected landmarks determined by the algorithm, the user had to click on the show corrected landmarks button. In addition, the sagittal and axial plane belonging to the 3D model could be shown and removed with the show plane and remove plane buttons.If a landmark was not positioned correctly, a landmark could be moved by dragging, or it could be deleted using the delete last placed landmark button, or delete all landmarks.

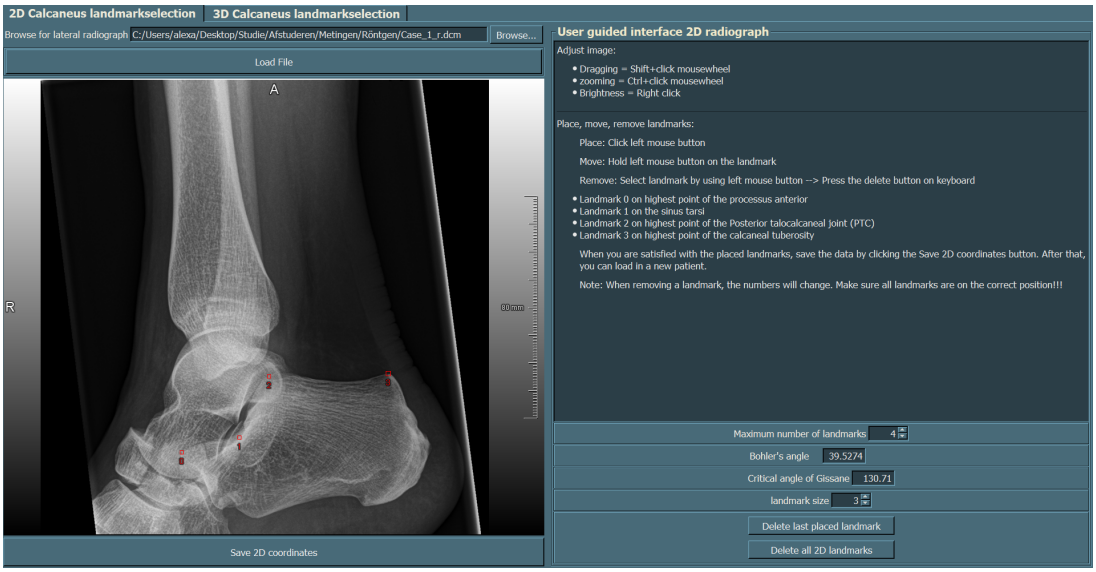

Figure 34: MeVisLab 2D measurement Graphical User Interface

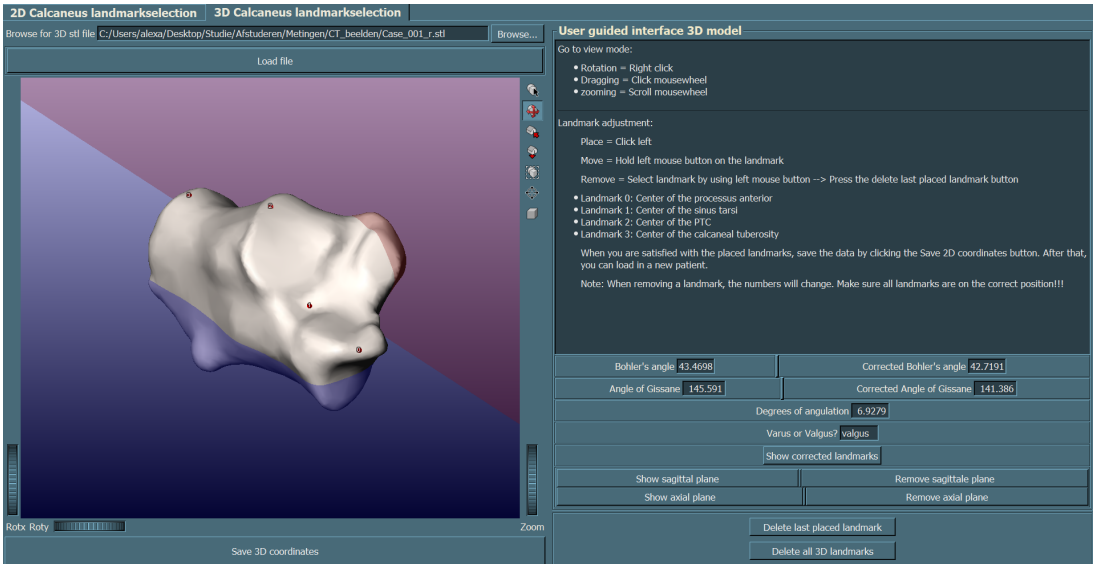

Figure 35: MeVisLab 3D measurement Graphical User Interface